Contents

Chapter 1

Theory

1.1 The shallow water equations

Free surface flows often appear in ocean, engineering and atmospheric modelling. In many applications involving unsteady water flows where the horizontal length scale is much greater than the vertical length scale, the shallow water equations (SWE) are commonly used to model these flows. These equations have been proposed by Saint-Venant [1] in 1871 to model flows in a channel. The SWE are derived from the three-dimensional Navier-Stokes equations for incompressible flows. A vertical integration is performed on the Navier-Stokes equations to obtain the set of two-dimensional SWE. The following hypotheses were made:

- Small bottom slope

- Hydrostatic distribution of the pressure

- The main motion of particles occurs in horizontal planes

- The vertical distribution of the horizontal velocity components u, v is nearly uniform

- The mass forces are gravity and the Coriolis force

- The vertical acceleration of the particles is negligible in comparison with the gravitational acceleration g

The two-dimensional SWE are a nonhomogeneous system of nonlinear hyperbolic equations and are expressed as

$$\frac{\partial \mathrm{U}}{\partial t} + \frac{\partial \mathrm{F(U)}}{\partial x} + \frac{\partial \mathrm{G(U)}}{\partial y} = \mathrm{S}, \qquad (x, y) \in \Omega, t \geq 0 \tag{1.1}$$

with the variable vector

$$\mathrm{U} = \begin{pmatrix} h \\ hu \\ hv \end{pmatrix} \tag{1.2}$$

where h is the water height and (u, v) the horizontal velocity components. These three variables are function of time t and horizontal space (x, y). The flux terms are expressed by

$$\mathrm{F(U)} = \begin{pmatrix} hu \\ hu^2 + \frac{gh^2}{2} \\ huv \end{pmatrix}, \qquad \mathrm{G(U)} = \begin{pmatrix} hv \\ huv \\ hv^2 + \frac{gh^2}{2} \end{pmatrix} \tag{1.3}$$

and the source term represents the combined effects of geometric slope S_0 and friction slope S_f

$$S = gh\left(S_0 + S_f\right) = -gh\begin{pmatrix} 0 \\ \frac{\partial z_b}{\partial x} \\ \frac{\partial z_b}{\partial y} \end{pmatrix} - gh\frac{n^2\sqrt{u^2 + v^2}}{h^{4/3}}\begin{pmatrix} 0 \\ u \\ v \end{pmatrix} \tag{1.4}$$

Herein g is the gravitational acceleration, $z_b(x, y)$ is the smooth topography and $n[m^{-1/3}s]$ is the Manning coefficient of roughness. The range of values for n spans from 0.01 glass) to 0.1 (flood plains reaching branches of trees), see Chow [2] (pages 109-113) for a compiled table of values.

This definition of the friction is common in many shallow water models: only the friction at the bottom of the bed is taken into account. Specifically models that assume vertical channel side-walls and use free-slip boundary conditions do not account for the friction at the walls. Neglecting this effect, open channel flow would likely show a marked variation in water depth from the one measured experimentally. Therefore an extension of the friction term (see Brufau [3]) has also been implemented:

$$ghS_f = -gh\sqrt{u^2 + v^2}\left(\frac{n_b^{3/2}}{h} + \frac{n_w^{3/2}l_w}{\Omega}\right)^{4/3}\begin{pmatrix} 0 \\ u \\ v \end{pmatrix} \tag{1.5}$$

Herein n_b and n_w are the Manning friction coefficients relative to the bottom and to the wall respectively. l_w is the length of the wall along the flow and Ω is the wetted area on the bottom near the wall.

The Froude number is defined as the ratio

$$Fr = \frac{\sqrt{u^2 + v^2}}{\sqrt{gh}} \tag{1.6}$$

and is analogous to the Mach number of gas dynamics. The wave speed $c = \sqrt{gh}$ is the velocity at which a disturbance should travel in the space. When $Fr < 1$, the flow is called *subcritical*. In this case, disturbances can travel upstream. On the other hand, when $Fr > 1$, the flow is called *supercritical*. In this case, the wave speed is smaller than the flow velocity and the disturbances can not travel upstream anymore.

1.2 Numerical discretization

The computational domain Ω is discretized into triangles of area Ω_i and the SWE are integrated over the whole domain.

1.2.1 The finite volume method

We assume here the cell-centered approach of the finite volume method. These cells are the same as the initial grid elements; the values of the dependent variables are averaged over the cell and can be stored in the cell center. The integration of the SWE (1.1) over the domain gives

$$\int_\Omega \frac{\partial U}{\partial t}d\Omega + \int_\Omega \frac{\partial F(U)}{\partial x}d\Omega + \int_\Omega \frac{\partial G(U)}{\partial y}d\Omega = \int_\Omega gh(S_0 + S_f)d\Omega \tag{1.7}$$

The computational domain is split into a set of finite volumes Ω_i and the divergence theorem is applied to the flux terms, turning the surface integrals into line integrals along the cell border Γ_i:

$$\int_{\Omega_i} \frac{\partial U}{\partial t}d\Omega_i = -\oint_{\Gamma_i}\left(n_xF(U) + n_yG(U)\right)d\Gamma_i + \int_{\Omega_i} gh(S_0 + S_f)d\Omega_i \tag{1.8}$$
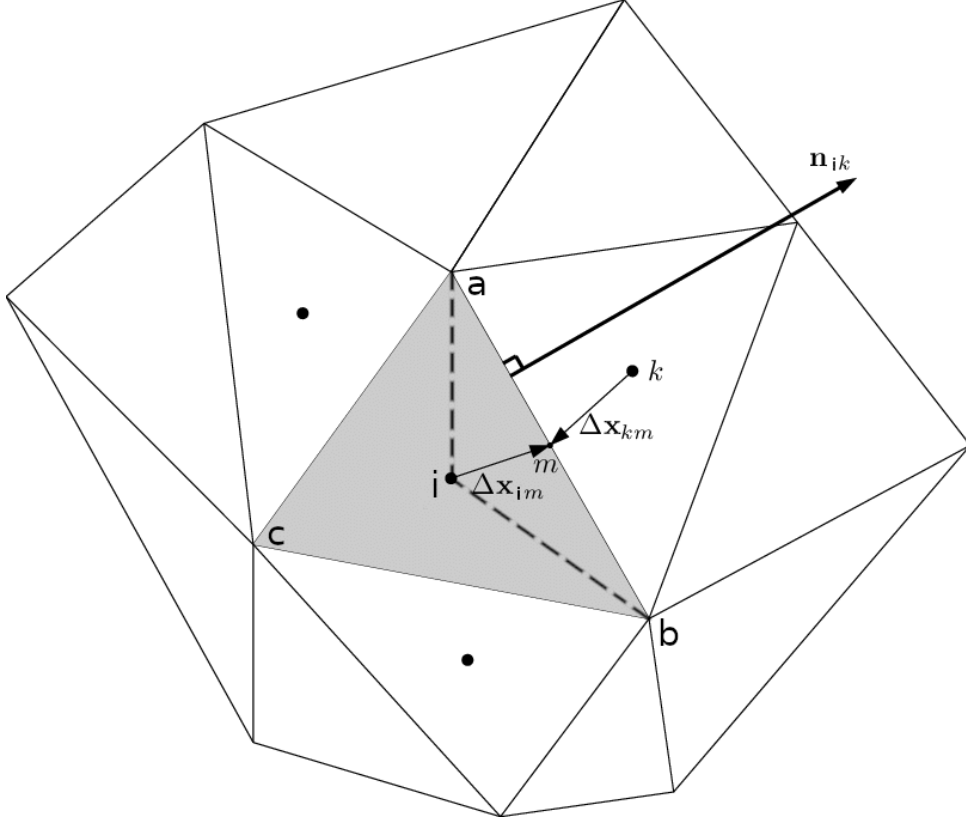
Figure 1.2.1: Cell-centered finite volume.

Herein (n_x, n_y) are the components of the normalized external normal to the edge of the cell. The physical interpretation of this results is the following. In an arbitrary domain, the rate of variation of the conservative variables U is given by the net flux towards the inside of the cell plus the variation generated by the source term.

The mesh is supposed to be freezed in space and the coordinates of the nodes are time-invariant. The temporal derivative is constant inside the cells and can go out of the surface integral. The previous result becomes

$$\frac{\partial U_i}{\partial t} = -\frac{1}{\Omega_i} \oint_{\Gamma_i} (n_x F(U) + n_y G(U)) \, d\Gamma_i + \frac{1}{\Omega_i} \int_{\Omega_i} gh(S_0 + S_f) d\Omega_i \qquad (1.9)$$

The discretization of the temporal term, the flux terms and the source term are set in the next three sections. The reader is referred to Fig. 1.2.1 for the definition of the geometrical inputs required by the cell-centered finite volume method.

1.2.2 Definition of the discretized flux

The line integral in Eq. (1.9) is split in a sum of integrals along each edge Γ_{ik} of the cell. In Fig. 1.2.1, the edges Γ_{ik} are the edges *abc*. Index i denotes the current cell and index k denotes the cell located on the other side of the edge Γ_{ik}.

$$\oint_{\Gamma_i} (n_x F(U) + n_y G(U)) \, d\Gamma_i = \sum_{k=1}^{3} \oint_{\Gamma_{ik}} \left(n_x^{ik} F(U) + n_y^{ik} G(U) \right) d\Gamma_i \qquad (1.10)$$

The sum is now expressed in terms of the variables at cells i and k using an upwind scheme. The van Leer Q-scheme [4] as implemented by Bermúdez [5]. Let us denote the two-dimensional flux

3

Z as

$$Z(U, n) = n_x \mathrm{F(U)} + n_y \mathrm{G(U)} \tag{1.11}$$

Then the Q-schemes are a family of upwind schemes in which the numerical flux through the edge ik is given by

$$\Phi_{ik}(U_i, U_k, n_{ik}) = \frac{Z(U_i, n_{ik}) + Z(U_k, n_{ik})}{2} - \frac{1}{2} |Q(U_m, n_{ik})| (U_k - U_i) \tag{1.12}$$

where U_i, U_k and U_m are the variables at cells i, k and the intermediate state $U_m = (U_i + U_k)/2$. The matrix Q is the Jacobian matrix of flux and is estimated at the intermediate state U_m.

$$\begin{aligned}
Q &= \frac{\mathrm{d}Z}{\mathrm{d}U} = n_x \frac{\mathrm{d}F}{\mathrm{d}U} + n_y \frac{\mathrm{d}G}{\mathrm{d}U} \\
&= \begin{pmatrix}
0 & n_x & n_y \\
n_x(-u^2 + gh) - n_y(uv) & 2n_x u + n_y v & n_y u \\
-n_x(uv) + n_y(-v^2 + gh) & n_x v & n_x u + 2n_y v
\end{pmatrix}
\end{aligned} \tag{1.13}$$

The system of equations is hyperbolic in the sense that the Jacobian matrix Q has real eigenvalues and a complete set of eigenvectors. Matrix $|Q|$ is obtained by

$$|Q| = X |\Lambda| X^{-1} \tag{1.14}$$

where X^{-1} is the matrix whose jth column is the jth right eigenvector of matrix Q. Λ is a diagonal matrix containing the absolute values of the eigenvalues λ_l ($l = 1, 3$). Let us denote $c = \sqrt{gh}$ the speed of the wave. The eigenvalues of the Jacobian matrix are

$$\begin{aligned}
\lambda_1 &= n_x u + n_y v \\
\lambda_2 &= \lambda_1 + c \\
\lambda_3 &= \lambda_1 - c
\end{aligned} \tag{1.15}$$

λ_2 and λ_3 are gravity waves while λ_1 is linearly degenerate. $|\Lambda|$, X and X^{-1} can be calculated

$$|\Lambda| = \begin{pmatrix}
|\lambda_1| & 0 & 0 \\
0 & |\lambda_2| & 0 \\
0 & 0 & |\lambda_3|
\end{pmatrix} \tag{1.16}$$

$$X = \begin{pmatrix}
0 & 1 & 1 \\
-n_y c & u + n_x c & u - n_x c \\
n_x c & v + n_y c & v - n_y c
\end{pmatrix} \tag{1.17}$$

$$X^{-1} = \frac{1}{2c} \begin{pmatrix}
2(n_y u - n_x c) & -2n_y & 2n_x \\
c - n_x u - n_y v & n_x & n_y \\
c + n_x u + n_y v & -n_x & -n_y
\end{pmatrix} \tag{1.18}$$

Finally the line integral (1.10) can be discretized by

$$\oint_{\Gamma_i} (n_x \mathrm{F(U)} + n_y \mathrm{G(U)}) \, \mathrm{d}\Gamma_i = \sum_{k=1}^{3} \oint_{\Gamma_{ik}} \left(n_x^{ik} \mathrm{F(U)} + n_y^{ik} \mathrm{G(U)} \right) \mathrm{d}\Gamma_i$$

$$\approx \sum_{k=1}^{3} \Phi_{ik} L_{ik} \tag{1.19}$$

where L_{ik} is the length of the edge between cells i and k.

1.2.3 Definition of the discretized source

1.2.3.1 Geometric slope

The contribution of the geometric slope to the surface integral of the source term in Eq. (1.9) is split in a sum of integrals over the three subcells iab, ibc and ica.

$$\int_{\Omega_i} gh\mathrm{S}_0 \mathrm{d}\Omega_i \approx \sum_{k=1}^{3} \varphi_{ik}\Omega_{ik} \tag{1.20}$$

The terms φ_{ik} and Ω_{ik} are respectively the approximated source term within each subcell and the area of these subcells. The convenience of upwinding the source term has been analyzed by Castro [6]. This use of this technique was justified in the case of one-dimensional problems as a means to avoid the propagation of spurious waves. In some sense, it was shown that the discretization of the source term should mimic that of the flux. The two-dimensional source in the three subcells iab, ibc and ica is approximated by

$$\varphi_{ik} = X(I - |\Lambda|\,\Lambda^{-1})X^{-1}\hat{S}_0 \tag{1.21}$$

Matrix I is the 3×3 identity matrix. Matrices X, X^{-1}, $|\Lambda|$ and Λ^{-1} are evaluated at the intermediate state U_m. The inverse eigenvalue matrix is given by

$$\Lambda^{-1} = \left(\begin{array}{ccc} 1/\lambda_1 & 0 & 0 \\ 0 & 1/\lambda_2 & 0 \\ 0 & 0 & 1/\lambda_3 \end{array}\right) \tag{1.22}$$

The term $|\Lambda|\,\Lambda^{-1}$ is thus equivalent to $sign(\Lambda)$, the matrix whose coefficients are the sign of the eigenvalues of matrix Q. The geometric source term $\hat{S}$ is approximated by

$$\hat{S}_0 \approx gh_m \frac{z_b^i - z_b^k}{\Delta x_{im}} \left(\begin{array}{c} 0 \\ n_x \\ n_y \end{array}\right) \tag{1.23}$$

where Δx_{im} is the distance between the cell center i and the mid-node m and z_b^i, z_b^k are the heights of the ground at cells i and k.

1.2.3.2 Friction slope

The contribution of the friction slope to the surface integral of the source term in Eq. (1.9) as given in Eq. (1.4) is evaluated by averaging the friction term over the cell:

$$\int_{\Omega_i} gh\mathrm{S}_\mathrm{f} \mathrm{d}\Omega_i \approx -gh_i\sqrt{u_i^2 + v_i^2}\frac{n^2}{h_i^{4/3}}\Omega_i \left(\begin{array}{c} 0 \\ u_i \\ v_i \end{array}\right) \tag{1.24}$$

The discretization of the extension of the Manning formula to take into account the wall friction (1.5) is given by

$$\int_{\Omega_i} gh\mathrm{S}_\mathrm{f} \mathrm{d}\Omega_i \approx -gh_i\sqrt{u_i^2 + v_i^2}\left(\frac{n_b^{3/2}}{h_i} + \sum_{j=1}^{3}\frac{\mu_{ij}n_w^{3/2}l_j}{\Omega_i}\right)^{4/3}\Omega_i \left(\begin{array}{c} 0 \\ u_i \\ v_i \end{array}\right) \tag{1.25}$$

Herein μ_{ij} equals 1 if side j of cell i is a wall, and equals 0 otherwise. l_j is the length of side j.
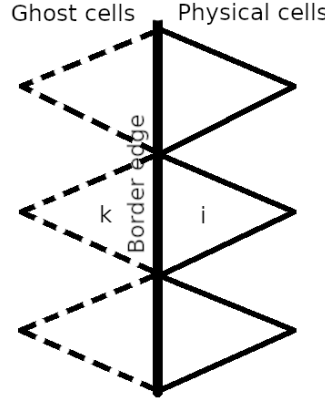
Figure 1.2.2: Definition of the ghost cells for imposing the boundary conditions.

1.2.4 Boundary conditions

The characteristic waves that propagate inside the domain have the Eigenvalues (1.15) as slopes. The number of incoming characteristics determine the number of boundary conditions to be set at each boundary edge. The flow regime (or the Froude number as defined in Eq. (1.6)) determines the number of incoming characteristics for each set of boundary edge. Knowing the number of imposed boundary conditions is a first step. A second step is the actual way to impose these conditions. In the finite volume methods, it is common to resort to *ghost cells* (see Fig.1.2.2) which will help to compute the required flux at the boundary edges. These ghost cells are artificial cells located on the other side of the border edge. They contain values U_k calculated in a way that the mean flux at the boundary edge is based on the imposed boundary values U_{BC}:

$$\Phi_{ik}(U_i, U_k, n_{ik}) = \frac{Z(U_i, n_{ik}) + Z(U_k, n_{ik})}{2} = Z(U_{BC}, n_{ik}) \tag{1.26}$$

These ghost cells have the same area as the physical cells attached to the common boundary edge. The upwinding method is applied for the flux but not for the source term. In the next subsections, it is supposed that $\lambda_1 > 1$, meaning that the flow enters for an inflow boundary and exits for an outflow boundary.

1.2.4.1 Inflow boundary condition

- A subcritical inflow has two incoming characteristics (λ_1 and λ_2 being positive and λ_3 being negative), and thus two boundary values must be imposed at the edge. These two values are chosen as the two components of the velocity vector (u_{BC}, v_{BC}). Thus the ghost cells contain the values

$$h_k = h_i \qquad u_k = 2u_{BC} - u_i \qquad v_k = 2v_{BC} - v_i$$

- A supercritical inflow has three incoming characteristics, and thus three boundary values must be imposed at the edge. These three values are chosen as the height h_{BC} and the two components of the velocity vector (u_{BC}, v_{BC}). Thus the ghost cells contain the values

$$h_k = 2h_{BC} - h_i \qquad u_k = 2u_{BC} - u_i \qquad v_k = 2v_{BC} - v_i$$

1.2.4.2 Outflow boundary condition

- A subcritical outflow has one incoming characteristics (λ_3), and thus one boundary value must be imposed at the edge. This value is chosen as the the height h_{BC}. Thus the ghost

cells contain the values

$$h_k = 2h_{BC} - h_i \qquad\qquad u_k = u_i \qquad\qquad v_k = v_i$$

- A supercritical outflow has zero incoming characteristics, and thus no boundary condition is imposed. The ghost cells contain the values

$$h_k = h_i \qquad\qquad u_k = u_i \qquad\qquad v_k = v_i$$

1.2.4.3 Slip-wall boundary condition

A slip-wall condition cancels the wall-normal velocity component and the velocity vector is parallel to the edge. Thus the ghost cells contain the values

$$h_k = h_i \qquad\qquad u_k = u_i - 2(un_x + vn_y)n_x \qquad\qquad v_k = v_i - 2(un_x + vn_y)n_y$$

1.2.4.4 Symmetry boundary condition

A symmetry boundary condition mirrors the values in cell i. Thus the ghost cells contain the values

$$h_k = h_i \qquad\qquad u_k = -u_i \qquad\qquad v_k = -v_i$$

1.2.5 Definition of the discretized time derivative

The spatial discretization of the flux Φ_{ik} and source φ_{ik} terms described in the two previous sections led Eq. (1.9) to the following result:

$$\frac{\partial U_i}{\partial t} = \frac{1}{\Omega_i}\left(\sum_{k=1}^{3} -\Phi_{ik}L_{ik} + \varphi_{ik}\Omega_{ik}\right) \qquad (1.27)$$

$$= f(U,t) \qquad (1.28)$$

Two time integration algorithms are implemented in the solver: the well-known fourth-order explicit Runge-Kutta method and the third order Total Variation Diminishing (TVD) explicit Runge-Kutta method.

1.2.5.1 Fourth-order explicit Runge-Kutta method

This method allows to reach a high accuracy in time while having a limit on the Courant-Friedrich-Lewy number (defined in Eq. (1.29)) which is higher than other standard methods.

$$\text{CFL} = \frac{\max(u)\Delta t}{\Delta x} \lesssim 2.8 \qquad (1.29)$$

In the case of a generic equation $\partial U_i/\partial t = f(U,t)$, the RK4 time integrator provides the next time step solution through

$$k_1 = \Delta t f(U^n, t^n)$$

$$k_2 = \Delta t f(U^n + \frac{k_1}{2}, t + \frac{\Delta t}{2})$$

$$k_3 = \Delta t f(U^n + \frac{k_2}{2}, t + \frac{\Delta t}{2})$$

$$k_4 = \Delta t f(U^n + k_3, t + \Delta t)$$

$$U^{n+1} = U^n + \frac{1}{6}(k_1 + 2k_2 + 2k_3 + k_4) \qquad (1.30)$$

1.2.5.2   Third order TVD explicit Runge-Kutta method

In Shu [7] a general TVD Runge-Kutta method is written under the form

$$U^{(i)} = \sum_{k=0}^{i-1} \left[\alpha_{ik} U^{(k)} + \beta_{ik} \Delta t f(U^{(k)}) \right], \qquad i = 1, m \tag{1.31}$$

The optimal third order scheme ($m = 3$) is given by

$$U^{(1)} = U^n + \Delta t f(U^n) \tag{1.32}$$
$$U^{(2)} = \frac{3}{4} U^n + \frac{1}{4} U^{(1)} + \Delta t f(U^{(1)})$$
$$U^{n+1} = \frac{1}{3} U^n + \frac{2}{3} U^{(2)} + \frac{2}{3} \Delta t f(U^{(2)})$$

The coefficients α_{ik} and β_{ik} are all positive, which ensures that the scheme is effectively TVD. Another clear advantage of this method is the low storage required to evaluate each substep.

1.2.6   Local time stepping

In case of steady flows, a local time stepping method is useful to accelerate the convergence towards the steady solution. The chosen local time step method within each cell is

$$\Delta t = \frac{\Omega \, \text{CFL}}{\sum_{j=1}^{3} \left| u n_x^j + v n_y^j \right| + cL} \tag{1.33}$$

where Ω is the area of the cell, (u, v) are the velocity components, $c = \sqrt{gh}$ is the wave speed, L is the perimeter of the cell and CFL is the Courant-Friedrich-Lewy number (defined in Eq. (1.29)).

Chapter 2

Verification of the code

2.1 Straight channel with slope and bottom friction

A straight channel with bottom slope and friction is first compared with the theoretical solution from gradually-varied flows in open channels. The width of the channel is $B_0 = 2m$, its length is $L = 1000m$ and its cross-section is rectangular. The mesh is composed of $1m$-side long right-angled triangles with a total of 4000 cells. The unit discharge is $q = Q/B_0 = 4m^2/s$ and two flow configurations (mild and steep slopes) were considered.

The numerical results are compared with the curves of the theory of gradually-varied flows in open channels. The reader is referred to Chow [2] and Chaudhry [8] for this theory. Two important parameters that drive the behaviour of the flow are the normal depth y_n and the critical depth y_c. The last one depends only on the geometry of the channel and is calculated through

$$y_c = \sqrt[3]{\frac{q^2}{g}} \tag{2.1}$$

The normal depth y_n is calculated in an iterative process by

$$Q = qB_0 = VA = \frac{A}{n}R^{2/3}\sqrt{S_0} \tag{2.2}$$

where $R = A/P$ is the hydraulic radius, $A = B_0 y_n$ is the cross-section area $P = B_0 + 2y_n$ is the wetted perimeter. The inputs of this equation are the Manning coefficient of roughness n, the geometrical slope S_0, the channel bottom width B_0 and the unit discharge q. The water level is also calculated in an iterative process by imposing a water level at one extremity of the channel and by computing the water slope with

$$\frac{dh}{dx} = \frac{S_0 - S_f}{1 - \frac{Q^2 B_0}{gA^3}} \tag{2.3}$$

where the friction slope $S_f = n^2 V^2 / R^{4/3}$. The standard step method described in Chow [2] and Chaudhry [8] is used to determine the water level at specified locations.

In the present configuration, it has been decided to neglect the friction coefficient of the side walls n_w and to keep only the friction at the bottom of the channel n_b. Indeed imposing a non zero friction coefficient n_w at the walls will induce subcritical areas in a globally supercritical flow. This will complicate the imposition of the boundary conditions at the exit (what value to impose for the height in these subcritical areas at the exit?) and the comparison with the theoretical curves (compare the theory with the average height profiles or at the centerline?). Therefore, in the following, a Manning coefficient n_b is chosen for the 2D computations and a

Mild slope		n_b	y_n	y_c
	2D shallow water	0.015	$1.579m$ measured	$1.1771m$
	1D	0.015	$2.394m$	$1.1771m$
	1D with n_e	0.0082	$1.4686m$	$1.1771m$
	1D with n_e manual	0.009	$1.579m$	$1.1771m$
Steep slope		n_b	y_n	y_c
	2D shallow water	0.01	$1.004m$ measured	$1.1771m$
	1D	0.01	$1.306m$	$1.1771m$
	1D with n_e	0.0067	$0.9353m$	$1.1771m$
	1D with n_e manual	0.00708	$1.004m$	$1.1771m$

Table 2.1: Straight channel with slope and bottom friction - Values for n_b, y_c and y_n for the 1D and 2D computations.

Manning coefficient n must be found so that the normal depths of both models match. Cueto-Felgueroso [9] compared 1D and 2D computations and also adapted the Manning coefficient for the 1D model. An equivalent Manning coefficient is calculated through

$$ n_e = \left(\frac{\sum P_i n_i^{3/2}}{\sum P_i} \right)^{2/3} = \left(\frac{B_0 n^{3/2}}{B_0 + 2y_n} \right)^{2/3} \tag{2.4} $$

The equivalent Manning coefficient is then used in conjunction with y_n in the iterative process of Eq. (2.2) and the water level through the standard step method. The calculated values are given in Table 2.1.

The two flow regimes calculated are based on the following parameters

- Mild slope $y_n > y_c$: the geometrical slope is $S_0 = 0.001$ and the Manning coefficient $n_b = 0.015$ for the 2D computations. For the theoretical 1D computation, the Manning coefficient must be adapted because the effect of friction is not taken into account along the side walls of the channel in the current implementation of the 2D shallow water solver ($n = 0$ along the walls). The Manning coefficient $n_b = 0.015$ used in the 2D solver leads to a too big theoretical y_n (in comparison with the measured one in the 2D solver). The equivalent Manning coefficient n_e calculated through Eq. (2.4) improved y_n but the difference is still too important. The manually chosen value $n_e = 0.009$ leads to the best fit between 1D and 2D and this value will be used for the 1D computation.

    As discussed in Section 1.2.4, subcritical flows are calculated by imposing the unit discharge q at the inlet and the water height h_{BC} at the outlet. Two cases are explored: case 1 with an imposed height $h_{BC} = 1.75m > y_n$ and case 2 with an imposed height $y_c < h_{BC} = 1.2m < y_n$. Doing so the mild-slope profiles M1 and M2 are selected. The supercritical profile M3 is not selected because it appears mostly behind partially opened sluice gates.

- Steep slope $y_n < y_c$: the geometrical slope is $S_0 = 0.002$ and the Manning coefficient $n_b = 0.01$ for the 2D computations. The Manning coefficient $n_b = 0.01$ used in the 2D solver leads to a too big theoretical y_n (in comparison with the measured one in the 2D solver). The equivalent Manning coefficient n_e calculated through Eq. (2.4) improved y_n but the difference is still too important. The manually chosen value $n_e = 0.00708$ leads to the best fit between 1D and 2D and this value will be used for the 1D computation.

    Three cases are explored: the subcritical case 3 with an imposed height $h_{BC} = 3.4m > y_c$ at the outlet and the supercritical cases 4 and 5 with an imposed height $y_n < h_{BC} =$

$1.15m < y_c$ and $h_{BC} = 0.7m < y_n$ respectively. The subcritical case 3 corresponds to the profile S1 and the supercritical cases 4 and 5 correspond to the profiles S2 and S3.
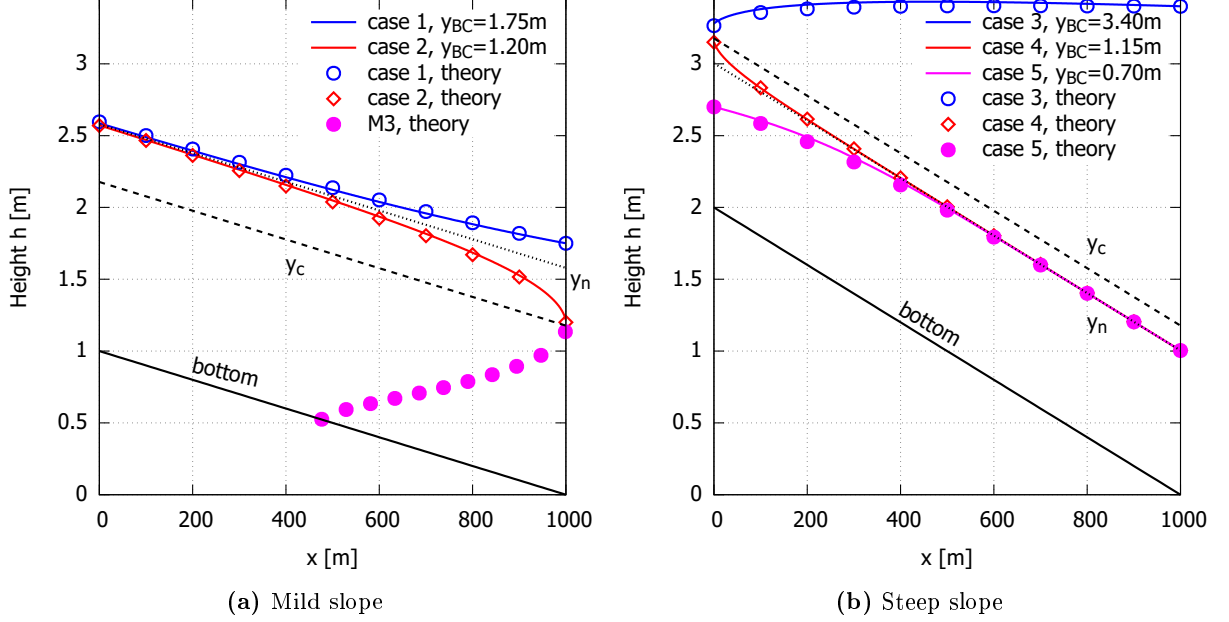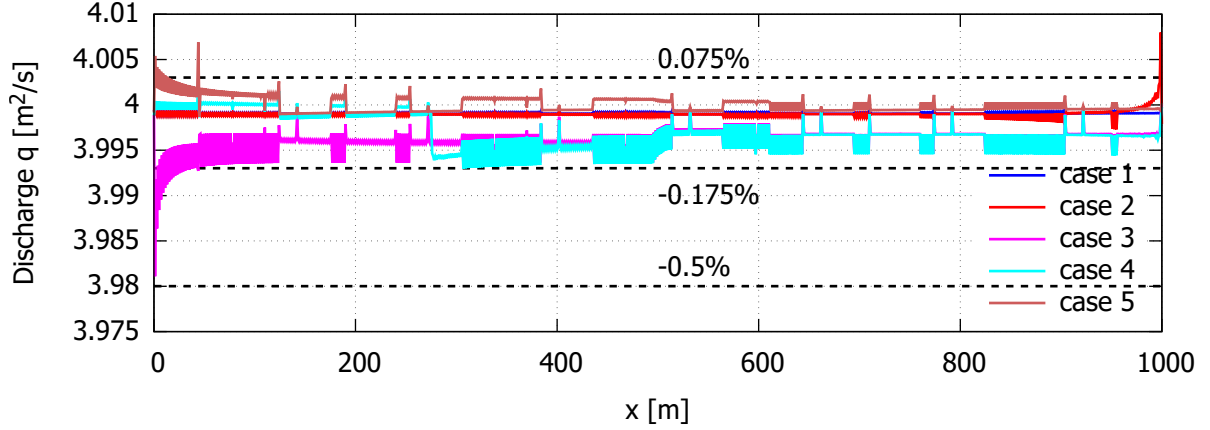

Figure 2.1.1: Straight channel with slope and bottom friction - Water levels in the case of a (left) mild slope and (right) steep slope. Comparison with the theoretical curves. The normal depth y_n and the critical depth y_c are depicted by dotted and dashed lines respectively

The water level at the centerline of the channel is plotted in Fig. 2.1.1 for both mild and steep slopes. A perfect matching with the theoretical curves is observed in every considered case. The normal depth is reached asymptotically whereas the critical depth is reached vertically. The water level in case 3 (=S1) tends to an horizontal asymptote. Indeed the analysis of Eq. (2.3) shows that for $h \to \infty$ then $Q \to 0$ and $S_f \to 0$ will means that $dh/dx \to S_0$. The theoretical supercritical profile M3 as been plotted in the case where $y_{BC} = 1.15m < y_c$. It is clear that such a profile can be computed by the shallow water solver only if the channel length $L < 523.2m$, location where the water level reaches the bottom of the channel. Case 3 has been particularly difficult to converge because of the upstream influence of the imposed water height. During the computation, the calculated water height at the inlet oscillated above and below the critical depth, changing the inlet from a supercritical to a subcritical boundary condition.

An important criteria to be respected by the numerical discretization is the conservation of the flowrate Q throughout the channel. Figure 2.1.2 shows the unit discharge $q = hu$ extracted from cuts perpendicular to the flow for the five cases. The maximum deviation from the nominal unit discharge is less than 0.5%, which shows a very good conservation of the flowrate.

This benchmark has allowed to validate the correct implementation of the source terms (both the geometrical and the friction slopes). This benchmark did not put forward any hydraulic jump where an important variation in height occurs in a short distance. Thus the stability of the Q-scheme has not been tested yet.

11

Figure 2.1.2: Straight channel with slope and bottom friction - Discharge $q = Q/B_0$ along the channel.

2.2 Straight channel with slope, bottom and wall friction

This section considers the same configuration as in the previous one with the addition of the side wall friction term (Eq. (1.5)). Now both the bottom n_b and side walls n_w Manning coefficients are taken into account by activating the corresponding parameters. The addition of friction along the walls will create a boundary layer-like behaviour. Thus the mesh must be adapted to this situation by increasing the number of elements along the direction perpendicular to the flow. The flow configuration is chosen similar to case 5 in Section 2.1. The flow will remain supercritical in overall with the exception of the subcritical region near to the walls. The width and length of the channel are $B_0 = 2m$ and $L = 1000m$, the geometrical slope is $S_0 = 0.002$, the unit discharge $q = Q/B_0 = 4m^2/s$, the Manning coefficients for the 2D computations are $n_b = n_w = 0.01$. At the inlet one imposes $h_{inlet} = 0.75m$ (supercritical) and at the outlet $h_{outlet} = 1.163235m$. This last value is active for the subcritical area near the side walls only. The theoretical curve for the height matches best the 2D results for $n_{th} = 0.0086$ (which is more comparable to the 2D value than in Section 2.1). This Manning coefficient for the 1D computation leads to a height $h_{outlet} = 1.163235m$ which was chosen as boundary value for the 2D computation.

Three cases were considered for the imposition of the velocity profile at the inlet: (case ①) an uniform one, (case ②) a second order one and (case ③) a fourth order velocity profile. Case ① gives directly $u_{inlet} = q/h_{inlet}$. Cases ② and ③ integrate the velocity profiles along the transverse direction in order to match the overall unit discharge $Q = qB_0 = h_{inlet} \int_0^{B_0} u(y) dy$. The boundary conditions on these profiles are $u_{inlet}(0) = u_{inlet}(B_0) = 0$ and $\partial u_{inlet}(B_0/2)/\partial y = 0$. For case ③ the additional condition is $\partial^2 u_{inlet}(0)/\partial y^2 = \partial^2 u_{inlet}(B_0)/\partial y^2 = \alpha$ controls the roundness of the profiles. The second order velocity profile is given by

$$u(y) = -\frac{6q}{h_{inlet}B_0^2}\left(y^2 - B_0 y\right) \tag{2.5}$$

and the fourth order velocity profile by

$$u(y) = ay^4 + by^3 + cy^2 + dy \tag{2.6}$$

$$a = \frac{5}{B_0^5}\left(\frac{B_0 q}{h_{inlet}} + \frac{\alpha B_0^3}{12}\right) \qquad\qquad b = -2aB_0$$

$$c = \frac{\alpha}{2} \qquad\qquad d = aB_0^3 - \frac{\alpha}{2}B_0$$

12

In the previous relation, parameter α has been chosen equal to -75. The three velocity profiles used in this configuration are shown in Fig. 2.2.1 as well as the corrected velocity profile extracted at the outlet of case $\textcircled{1}$.
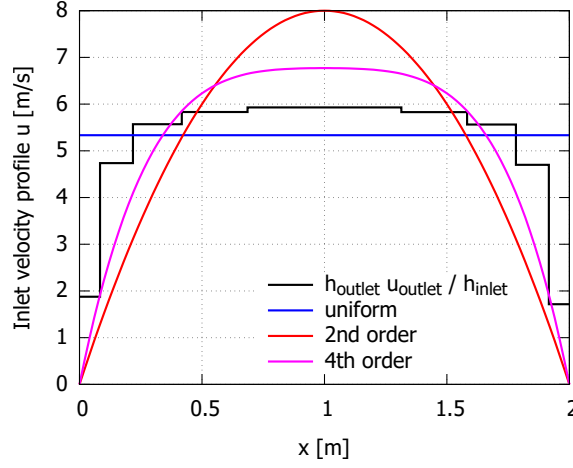
Figure 2.2.1: Straight channel with slope, bottom and wall friction - Several velocity profiles imposed at the inlet. The black line represents the velocity profile from the outlet of the 2D model with uniform inlet corrected for the inlet condition.

Figure 2.2.2 shows the magnitude of the velocity at the inlet and outlet of the channel for case $\textcircled{1}$. One clearly sees the progressive development of the boundary layer at the inlet whereas it is completely developed at the outlet.
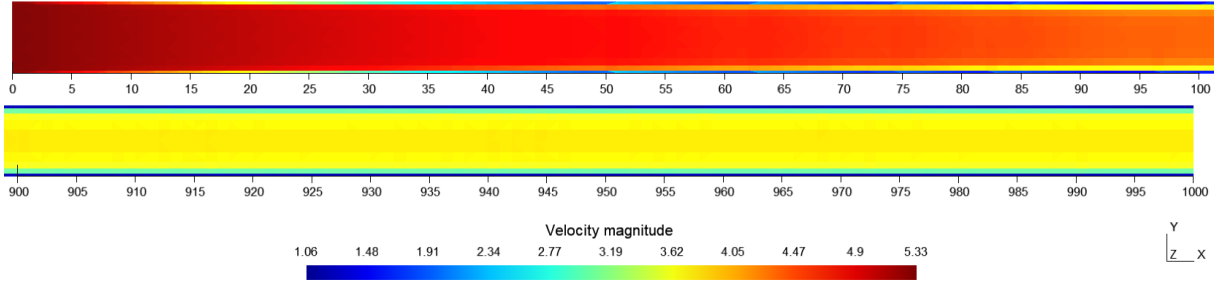
Figure 2.2.2: Straight channel with slope, bottom and wall friction - Development of the boundary layer (top) at the inlet and (bottom) at the outlet.

Figure 2.2.3 shows the height and Froude number along cuts at the wall and at the centerline. The theoretical 1D curves are also depicted for comparison. The height is more or less uniform along the direction perpendicular to the flow. Because of the variation of the velocity profile and because the unit discharge must be conserved, the Froude number also displays a varying shape along the direction perpendicular to the flow. A subcritical area is indeed observed near the wall and a supercritical core allows to ensure the conservation of the flow rate. For case $\textcircled{1}$ a very good agreement is reached for the height after that the boundary layer has been developed ($x > 200m$). In the region $x < 200m$, the water level predicted by the 2D model overshoots the theoretical one because of the global deceleration of the flow. An unsteadiness also appears, triggered by fluctuations inside the boundary layer. Cases $\textcircled{2}$ and $\textcircled{3}$ do not show the overshoot at the beginning of the channel but are slower to converge towards the theoretical value. The Froude number converges faster than case $\textcircled{1}$ at the wall but slower at the centerline.

In opposition to the case where the side wall friction was neglected, the evolution of the

13

(a) Height
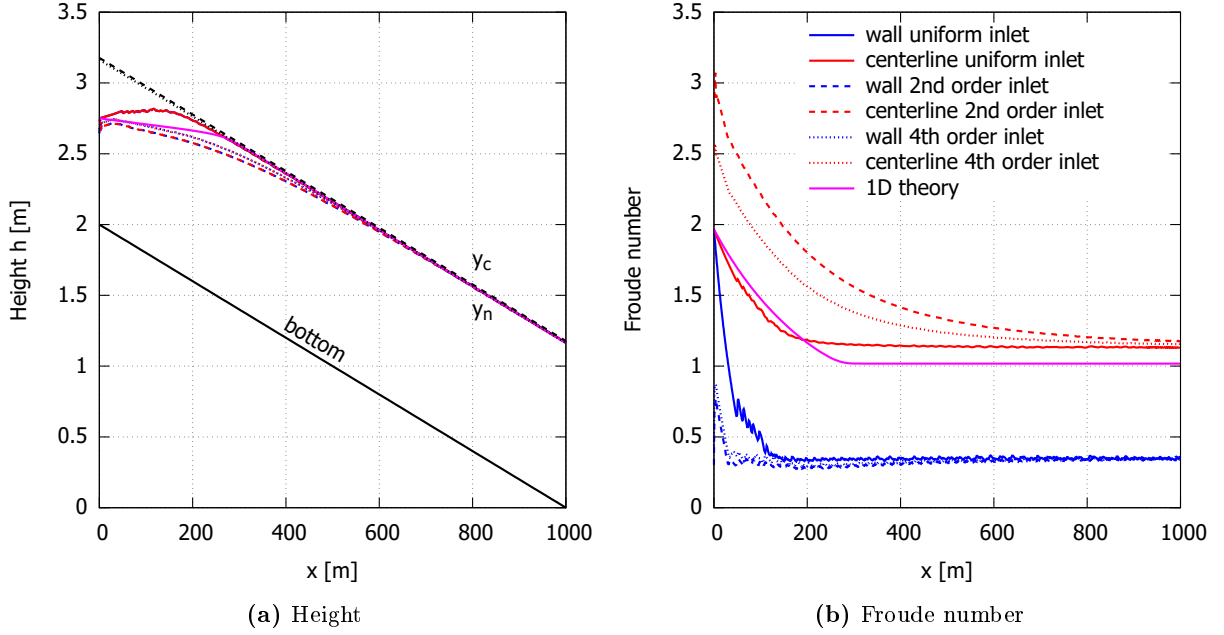
(b) Froude number

Figure 2.2.3: Straight channel with slope, bottom and wall friction - (left) Water levels and (right) Froude number. Comparison with the theoretical curves. The normal depth y_n and the critical depth y_c are depicted by dotted and dashed lines respectively
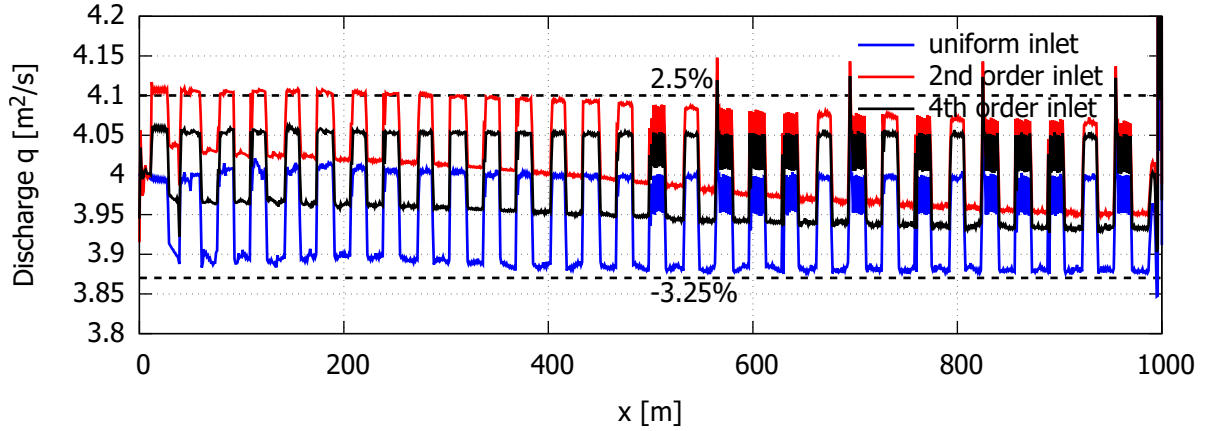

Figure 2.2.4: Straight channel with slope, bottom and wall friction - Discharge $q = Q/B_0$ along the channel.

flowrate along the channel shows a more pronounced deviation from the imposed value (see Fig. 2.2.4). Case ① shows an error between -3.25% and 0.5%, case ② shows an error between -1.25% and 2.5% and case ③ shows a more symmetrical error between -1.25% and 1.25%.

2.3 Oblique hydraulic jump

A supercritical flow is deflected inwards by a vertical boundary (slope θ, see Fig.2.3.1). No bathymetric variation is present in the flow. Slip-wall boundary conditions are imposed on the top and bottom parts of the flow. The initial height of the flow h_1 increases abruptly to a height h_2 along a wavefront which extends from the point of boundary discontinuity C at a wave angle

14
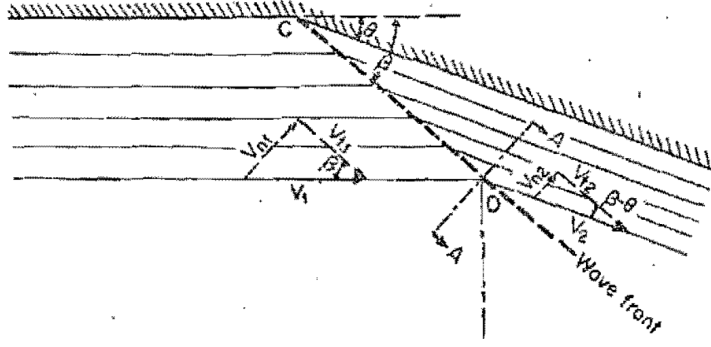
Figure 2.3.1: Oblique hydraulic jump

β. The magnitude of β depends partially on the angle θ. When $\theta = 0$, one retrieves the normal hydraulic jump with the wavefront perpendicular to the direction of flow ($\beta = 90 \deg$). By imposing values for θ and the Froude number $Fr_1 = v_1/\sqrt{gh_1}$ upstream of the jump, the wave angle β can be calculated by iteration on the following relation (see Chow [2]):

$$\tan \theta = \frac{\tan \beta \left(\sqrt{1 + 8Fr_1^2 \sin^2 \beta} - 3 \right)}{2 \tan^2 \beta + \sqrt{1 + 8Fr_1^2 \sin^2 \beta} - 1} \tag{2.7}$$

Then the height h_2 and the amplitude of the velocity u_2 downstream of the jump can be retrieved by the relations

$$h_2 = h_1 \frac{\tan \beta}{\tan (\beta - \theta)} \tag{2.8}$$

$$v_2 = v_1 \frac{\cos \beta}{\cos (\beta - \theta)} \tag{2.9}$$

Yoon and Kang [10] and Valiani *et al.* [11] also used this test case as a benchmark for their codes.

The inflow Froude number is chosen in a way that the flow remains supercritical behind the jump. The chosen flow parameters are

$$\theta = 10 \deg \qquad h_1 = 1.0 \qquad u_1 = 9.0 \qquad Fr_1 = 2.8735 \tag{2.10}$$

With the help of Eqs. (2.7)- (2.9), this leads to

$$\beta = 29.882 \deg \qquad h_2 = 1.5889 \qquad u_2 = 8.2981 \qquad Fr_2 = 2.1018 \tag{2.11}$$

A set of uniform meshes of triangles are built, see Fig. 2.3.2 for one example. The horizontal and vertical sides of the triangles on the inflow boundary have the same length. This length is used as the characteristic length of the mesh during the study of the convergence rate later in this section. The wavefront will cut through cells so that a region of transition will exist between the upstream and downstream solutions. As the solution is steady, a local time step is calculated for each cell.

The left part of Fig. 2.3.3 shows the converged height. Two major observations can be made. First the solution is homogeneous upstream and downstream of the jump. Secondly the location of the wavefront coincides with the theoretical one. A region of transition exists around the wavefront because the wavefront cuts through the cells. No spatial oscillation is observed inside the solution, specially around the wavefront. The relative error $\epsilon = \sqrt{\sum_i^N (h_i - h_{th})^2}/\sqrt{\sum_i^N h_{th}^2}$

15

(a) Coarse mesh   (b) Finer mesh
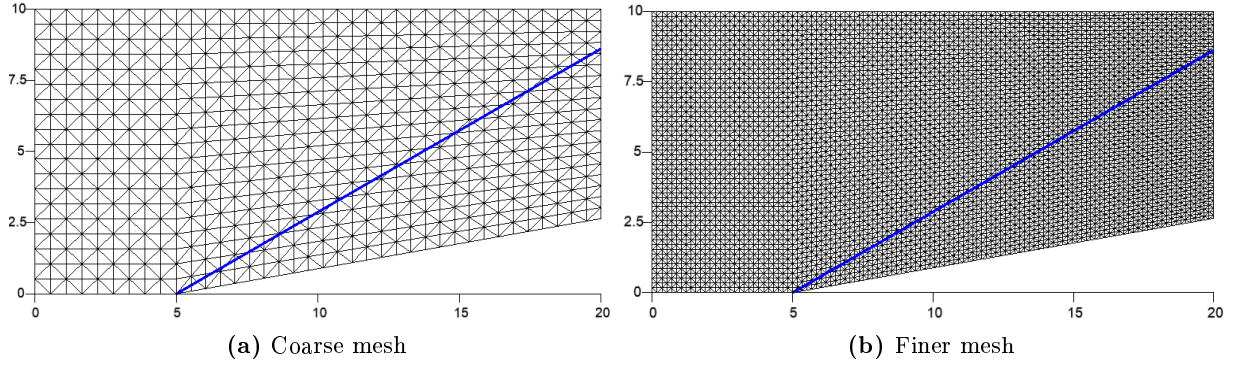
Figure 2.3.2: Oblique hydraulic jump - Uniform mesh used to test the convergence rate. The wavefront with $\beta = 29.882\,\mathrm{deg}$ is depicted by the blue line.

(a) Converged height   (b) Relative error
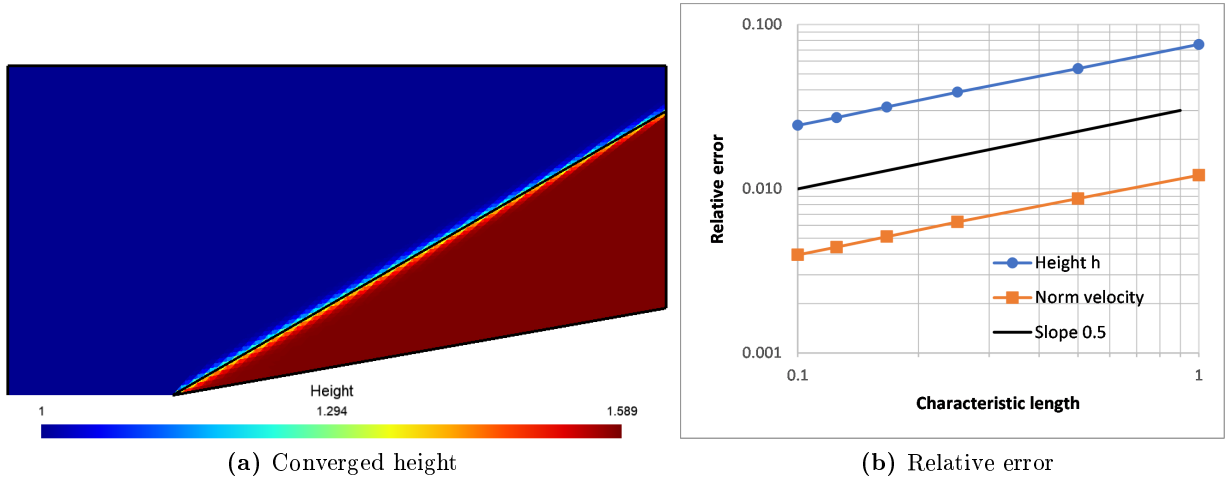
Figure 2.3.3: Oblique hydraulic jump - (left) Spatial distribution of the height h. The wavefront with $\beta = 29.882\,\mathrm{deg}$ is depicted by a black line. (right) Convergence rate of the height and norm of the velocity.

can be calculated for both the height and the norm of the velocity. The characteristic length of the mesh is chosen equal to the length of the vertical sides of the triangles on the inflow boundary. By changing the number the number of elements along the inflow boundary, the number of cells along the horizontal direction is automatically adapted. The right part of Fig. 2.3.3 shows the convergence of the relative errors. The calculated convergence rate is close to 0.5 in the log-log space for both curves.

2.4   Supercritical flow in symmetrical contraction

2.4.1   Bed slope and friction are neglected

Channel transitions should be designed to accomplish the necessary change in cross-section with as little flow disturbance as possible. In supercritical flows the standing waves produced by changes of direction in and downstream from the transition. In the present case the rectangular channel transition depicted in Fig. 2.4.1 has been chosen. The maximum flow disturbance results when the initial wave front intersection (point B) occurs at the downstream transition CC'. When the reflected waves BD and BD' intersect the channel walls below or above section CC', diamond-
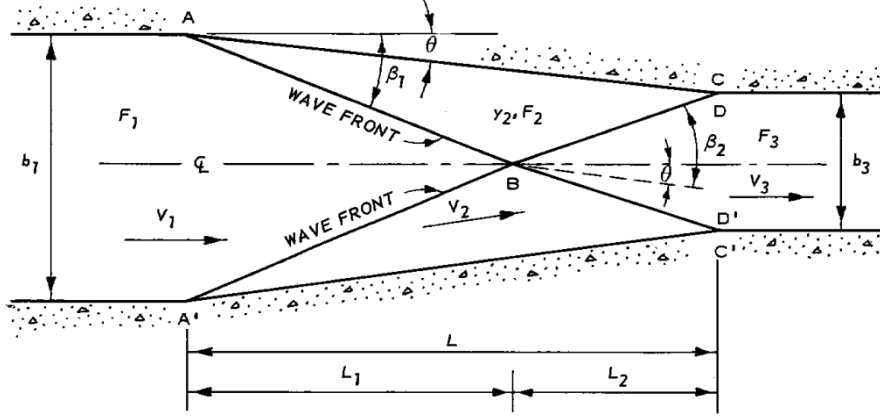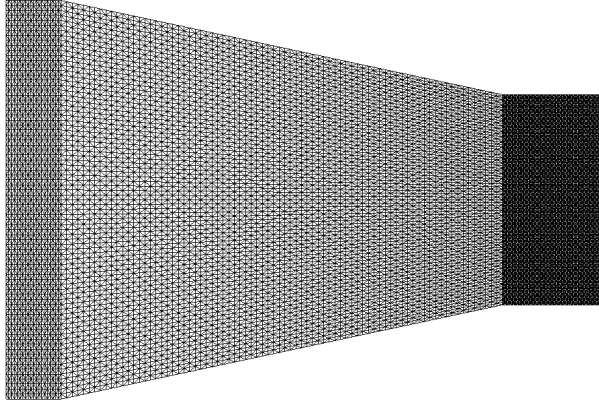
Figure 2.4.1: Supercritical flow in symmetrical contraction, picture from [12]

shaped cross waves develop in the channel. However, the change in wall alignment at section CC' results in negative wave disturbances that should tend to decrease the downstream effects of positive wave fronts. This should result in somewhat lower depths where the waves meet the downstream walls. The minimum disturbance occurs when the reflected waves BD and BD' meet the channel walls at section CC'. This, theoretically, results in the flow filaments again becoming parallel to the channel centerline. The surface disturbances are thus minimized when $L = L_1 + L_2$. If the reflected waves meet the walls upstream from section CC', the waves would be deflected again with a resulting increase in depth.

$$L_1 = \frac{b_1}{2 \tan \beta_1} \qquad\qquad L_2 = \frac{b_3}{2 \tan(\beta_2 - \theta)} \qquad\qquad (2.12)$$

Lai and Chan [13] chose the following parameters for the geometry: channel widths $b_1 = 20m$ and $b_3 = 10.548m$, length of the contraction $L = 22.233m$ for a wall deflection angle $\theta = 12 \deg$. The inflow Froude number is $\mathrm{Fr}_1 = 2.7$ and the inflow water level is $h_1 = 1m$. The wave angles calculated from relation 2.7 are $\beta_1 = 33.6879 \deg$ and $\beta_2 = 48.1022 \deg$. The lengths given in Eq. (2.12) are $L_1 = 15.0012m$ and $L_2 = 7.2319m$. In region 2, the water level is $h_2 = 1.676m$, the amplitude of the velocity is $v_2 = 7.5726m/s$ and the Froude number is $\mathrm{Fr}_2 = 1.7875$. In region 3, the water level is $h_3 = 2.5618m$, the amplitude of the velocity is $v_3 = 6.2589m/s$ and the Froude number is $\mathrm{Fr}_3 = 1.2485$.

Two steady computations were run on different type of meshes, see the top part of Fig. 2.4.2. A first uniform mesh of nearly 30.000 cells and a second non-uniform mesh of nearly 20.000 cells. The second one has been designed on the basis of the knowledge of the theoretical values of β_1, β_2, L_1 and L_2. Despite the higher number of cells, the uniform mesh fails at predicting the correct water level in region 3. Indeed the reflected wave front coming from the first intersection at L_1 misses by little the exact location of L_2. This generates diamond-shaped cross waves in the channel downstream which reflects against the walls and intersects themselves. On the other side, despite having less cells, the non-uniform mesh predicts the correct value for L_2 and no additional reflection is generated downstream. The correct theoretical water levels are computed in the three regions by the non-uniform mesh. No overshoot or oscillation are observed in the vicinity of the jumps; this indicates the validity and the robustness of the numerical method implemented in the present solver.
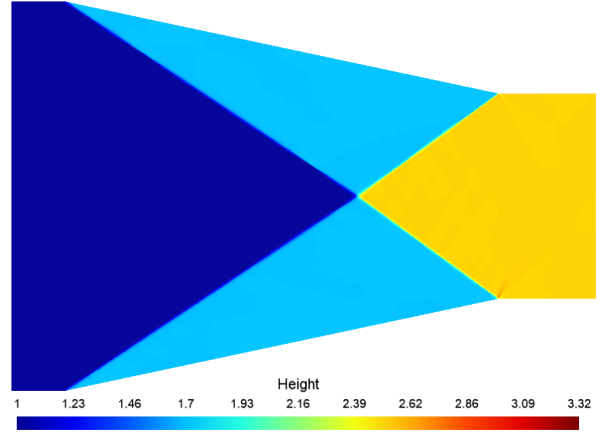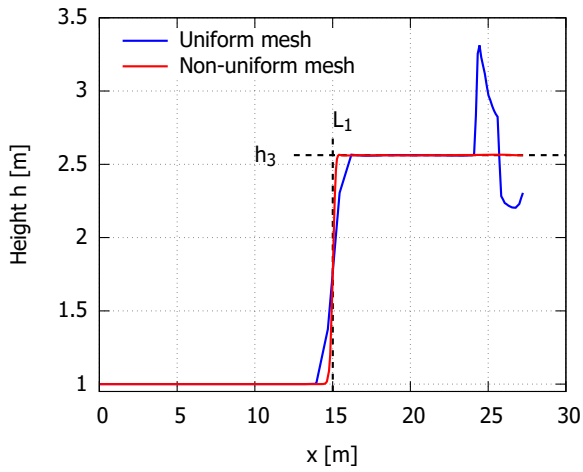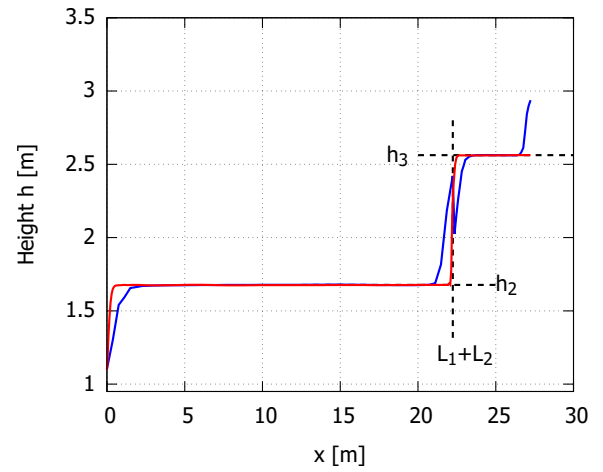
17
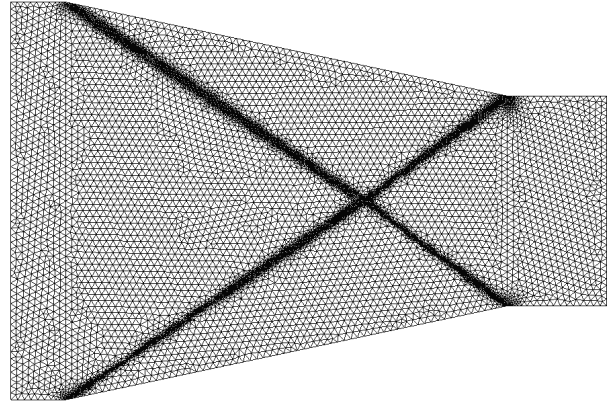
(a) Uniform mesh

(b) Non-uniform mesh
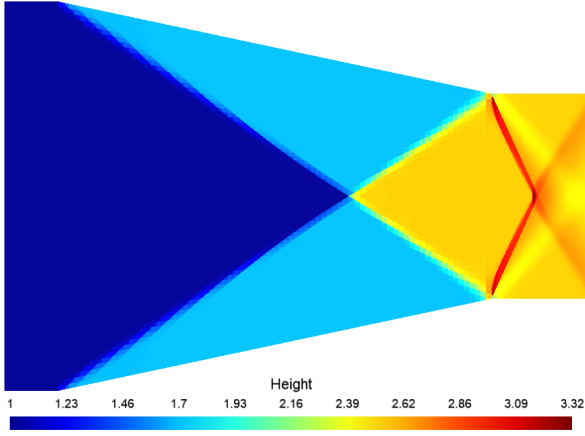
(c) Water level with uniform mesh

(d) Water level with non-uniform mesh

(e) Water level along the centerline

(f) Water level along the wall

Figure 2.4.2: Supercritical flow in symmetrical contraction - [top] Meshes used for the two computations and [middle and bottom] their respective water levels.

2.4.2 Bed slope and friction are taken into account

Other researchers studied the same flow topology with inclusion of the bed slope and the roughness (see e.g. Berger [14], Chaudhry [8] and Lee [15]). These studies are based on the experimental setup of Ippen [16]. The dimensions of the channel were $b_1 = 2ft$, $b_3 = 1ft$ and $L = 4.78ft$ (angle $\theta = 6\deg$). The inflow conditions are $\mathrm{Fr}_1 = 4.$ and $h_1 = 0.1ft$. The bed slope is $S_0 = 0.05664$ and the Manning coefficient of roughness $n = 0.0107m^{1/3}/s$.

A non-uniform mesh has been built on the basis of a first solution computed on an uniform mesh. The extraction of the gradient in water level allowed the generation of refined areas thanks to the mesh generator Gmsh [17]. An example of such a mesh is shown on the top part of Fig. 2.4.3. By neglecting the bed slope and the friction, the theoretical values for β_1, β_2, L_1 and L_2 were computed:

$$\beta_1 = 19.68\deg \qquad\qquad \beta_2 = 23.59\deg \tag{2.13}$$
$$L_1 = 0.8523m \qquad\qquad L_2 = 0.4808m \tag{2.14}$$
$$h_2 = 0.147ft \qquad\qquad h_3 = 0.2024ft \tag{2.15}$$
$$\mathrm{Fr}_2 = 3.178 \qquad\qquad \mathrm{Fr}_3 = 2.703 \tag{2.16}$$

These values were naively depicted on Fig. 2.4.3. One observes two things:

- The effect of the bed slope and friction taken into account during the generation of the mesh shifts the first intersection between the wave fronts upstream in comparison with the theory (red curves).

- The intersection of the reflected waves with the walls occurs upstream of section of section CC' (Fig. 2.4.1) where the converging channel reverts to parallel walls. Diamond-shaped cross waves will thus be generated downstream of section CC'.

The bottom part of Fig. 2.4.3 shows the water level of the computation that includes the geometrical and friction slopes. One clearly see the generation of the oblique shock waves on each side of the contraction, their interaction and their reflection on the walls. One also clearly sees the generation of the diamond-shaped cross waves downstream of CC' as explained above. Because no free-access is granted to the work of Ippen [16], it can not be checked whether this last effect was desired or not. However all the succeeding studies (Berger [14], Chaudhry [8] and Lee [15]) also put forward the generation of diamond-shaped cross waves in region 3.

The variation in height along the centerline and along the lateral walls is shown in Fig. 2.4.4. The height has been made non-dimensional by the height h_1 at the entry of the channel. Both computations (with and without bed slope and friction) provide similar shapes in comparison with the numerical results from Chaudhry [8]. The locations of the jumps are similar and one clearly see the constant level of the height in the area away from the jumps, in the case where the slopes are neglected. If both slopes are takes into account, then a slight increase in height takes place as the water moves downstream. The addition of the roughness dampens the peaks where the walls are parallel again. A very good agreement is met with the theoretical values for the computation without bed slope or friction.

The behaviour of the water surface in this supercritical flow scenario is quite sensitive to bottom friction. Figures 2.4.5 and 2.4.6 show the water surface level using several values of the Manning coefficient ($n = 0.011$, 0.013 and 0.015) at constant bed slope $S_0 = 0.05664$. Theoretical results from the Bresse's extension of Eq. (2.3) to nonprismatic geometries of the 1D momentum equation (see Eq. (2.17)) are also given for comparison. The 2D shallow water theory predicts a complex pattern of oblique standing waves, while the 1D theory yields gradually varied supercritical flow throughout. Qualitatively, both the 1D and 2D models capture the overall water
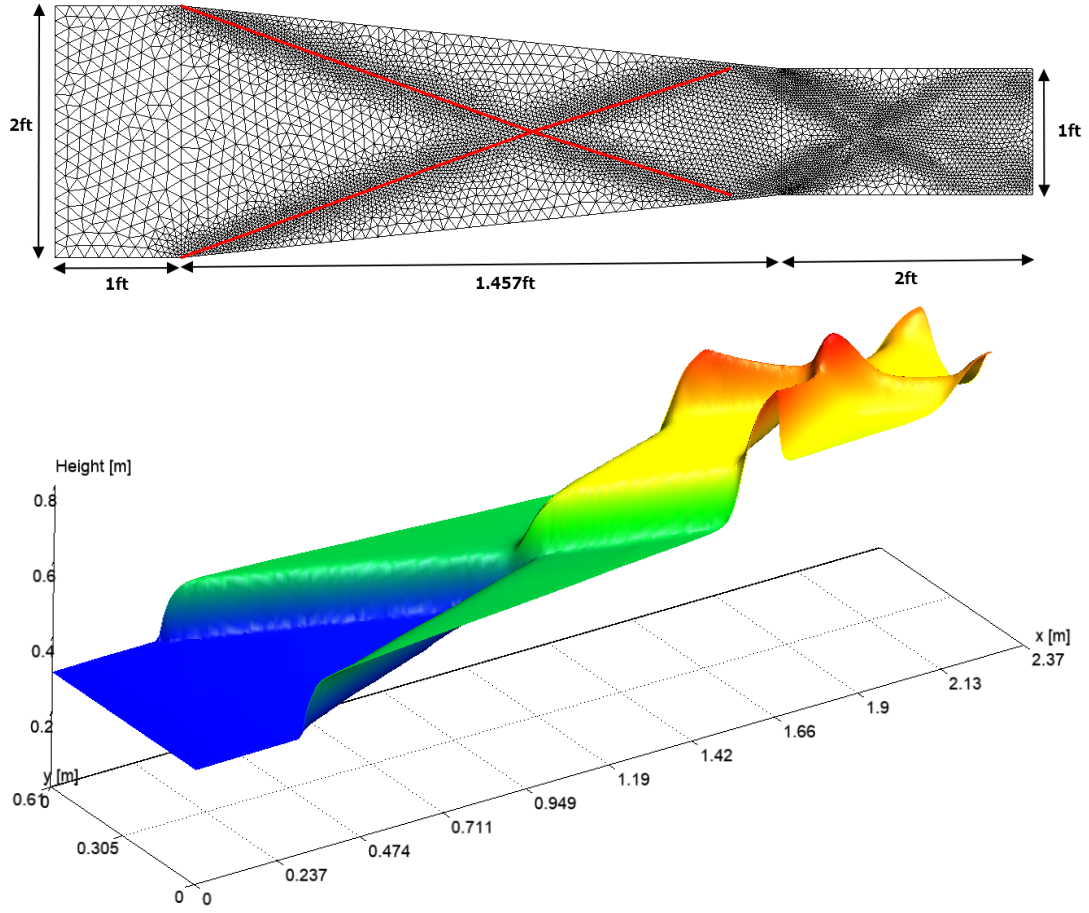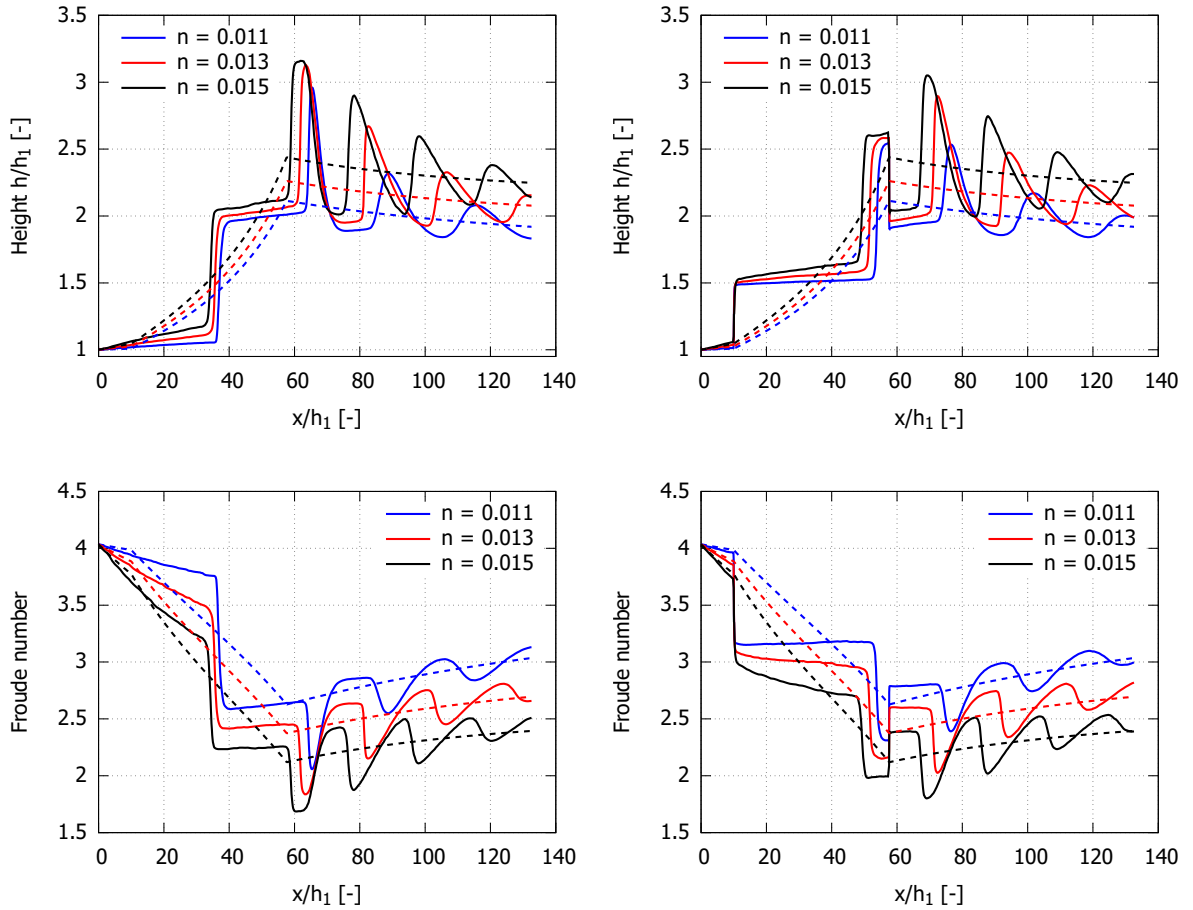
Figure 2.4.3: Supercritical flow in symmetrical contraction including bed slope and friction - [top] Geometry and mesh generated by Gmsh [17] and [bottom] water level for $S_0 = 0.05664$ and $n = 0.0107$.
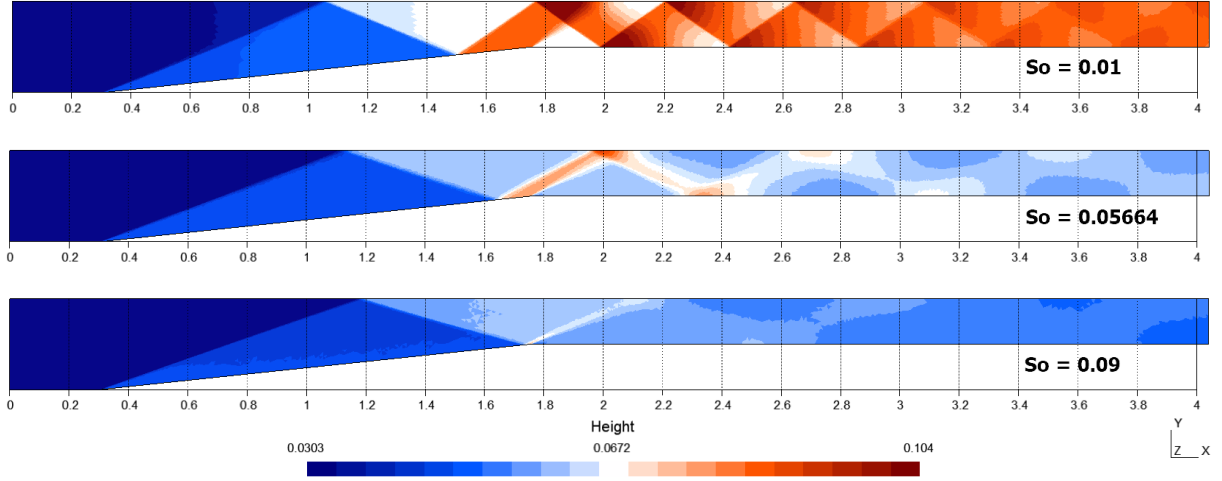

(a) Along the centerline
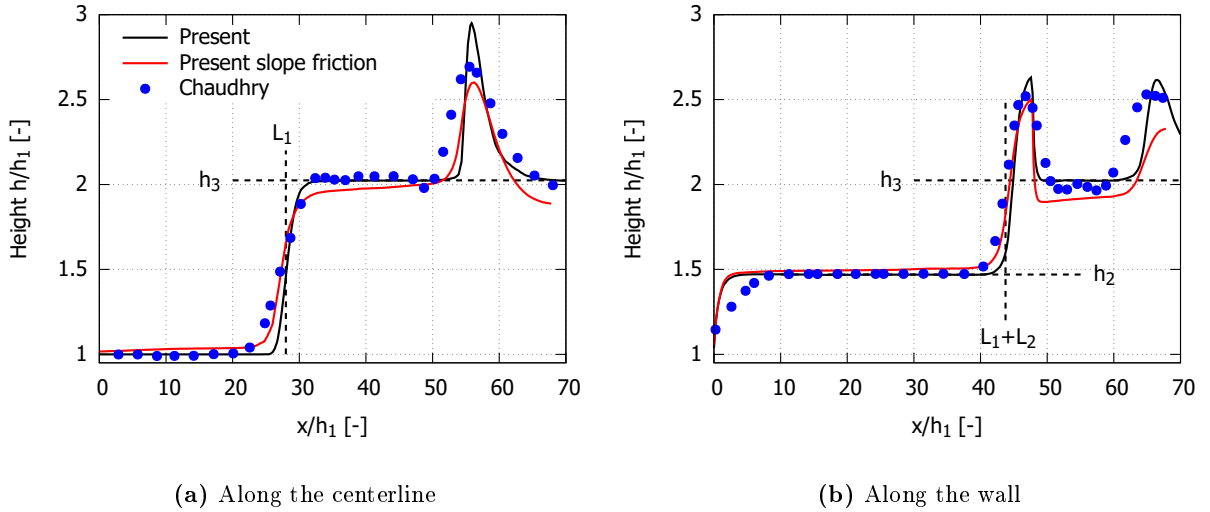
(b) Along the wall

Figure 2.4.4: Supercritical flow in symmetrical contraction including bed slope and friction - Water level along the centerline and along the wall. The numerical results from Chaudhry [8] are put for comparison. The geometrical/friction slopes ($S_0 = 0.05664$ and $n = 0.0107$) are included in the red curves but not in the black ones.
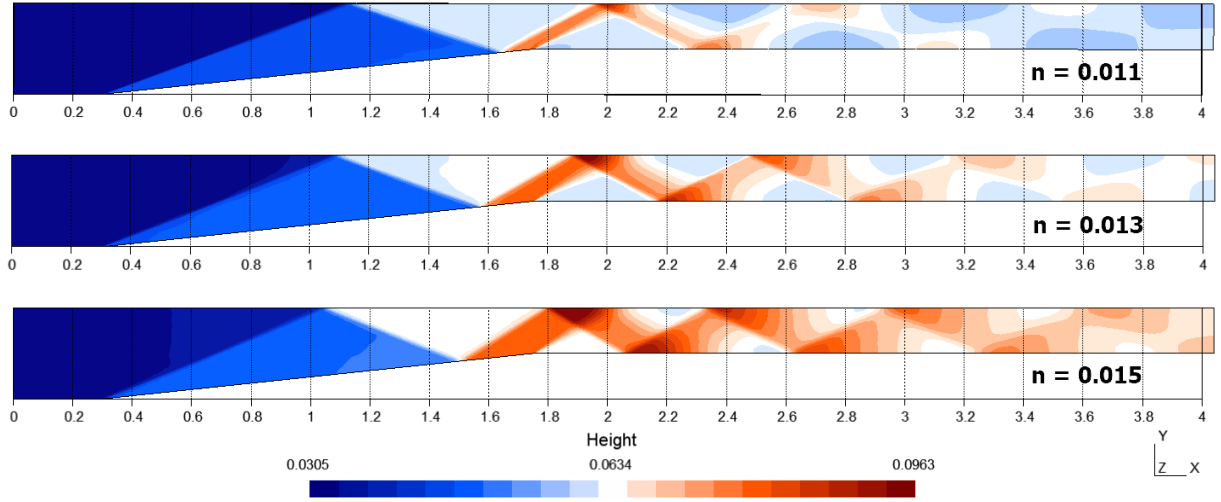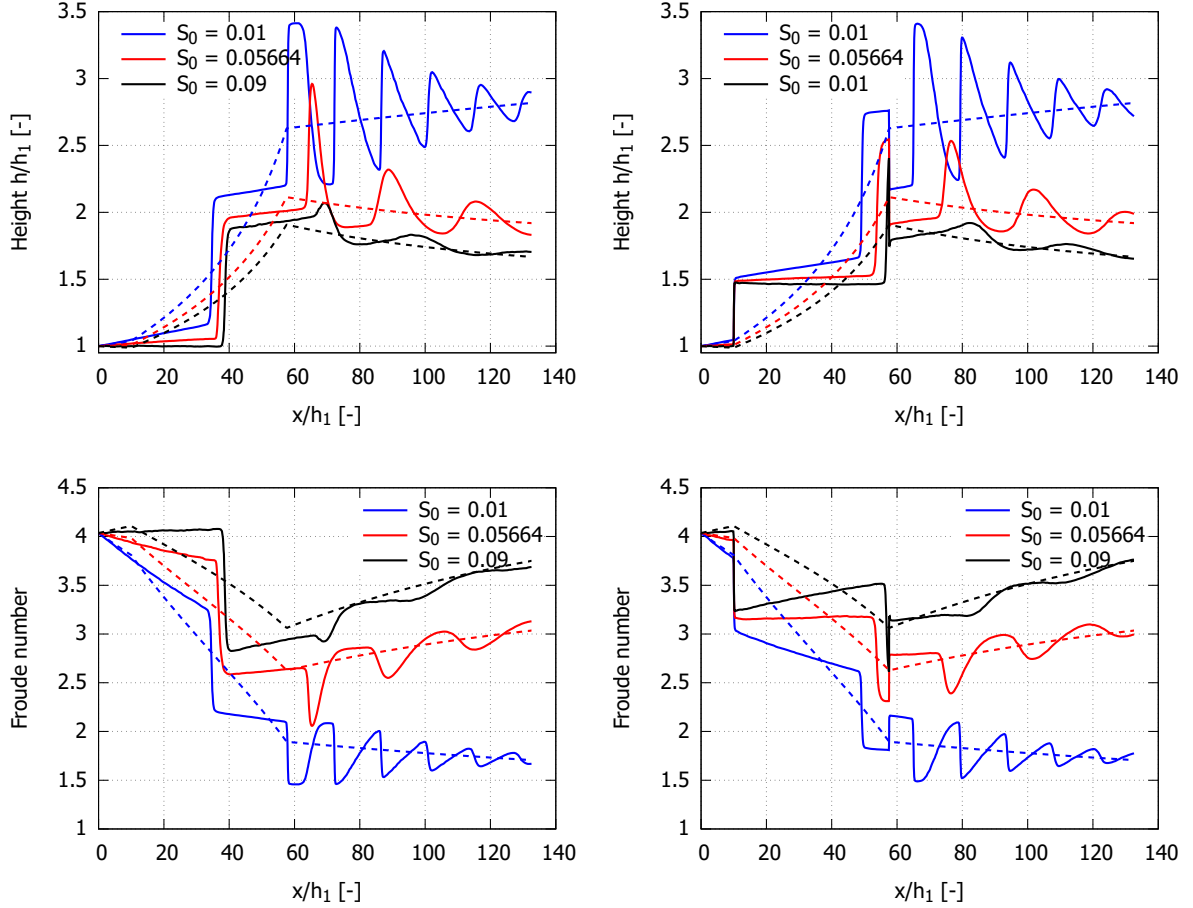
Figure 2.4.5: Supercritical flow in symmetrical contraction including bed slope and friction - Influence on the solution of the friction coefficient for constant bed slope ($S_0 = 0.05664$). From top to bottom $n = 0.011$, 0.013 and 0.015.

Figure 2.4.6: Supercritical flow in symmetrical contraction including bed slope and friction - Influence on the solution of the friction coefficient for constant bed slope ($S_0 = 0.05664$). (left) Along the centerline and (right) along the wall. (top) Water level h and (bottom) Froude number. (full lines) 2D shallow water model and (dashed lines) Bresse's extension of Eq. (2.3) to nonprismatic geometries of the 1D momentum equation (Eq. (2.17)).

Figure 2.4.7: Supercritical flow in symmetrical contraction including bed slope and friction - Influence on the solution of the friction coefficient for constant Manning friction coefficient ($n = 0.011$). From top to bottom $S_0 = 0.01$, 0.05664 and 0.09.

Figure 2.4.8: Supercritical flow in symmetrical contraction including bed slope and friction - Influence on the solution of the friction coefficient for constant Manning friction coefficient ($n = 0.011$)). (left) Along the centerline and (right) along the wall. (top) Water level h and (bottom) Froude number. (full lines) 2D shallow water model and (dashed lines) Bresse's extension of Eq. (2.3) to nonprismatic geometries of the 1D momentum equation (Eq. (2.17)).

surface profile along the centerline and along the wall. An increase in the friction coefficient leads to an increase of the initial wave angle ($\beta \approx 20.3\,\mathrm{deg}$ for $n = 0.011$, $\beta \approx 21.2\,\mathrm{deg}$ for $n = 0.013$ and $\beta \approx 22.5\,\mathrm{deg}$ for $n = 0.015$). This implies that, at high friction coefficients, the hydraulic jump hits the wall for the first time more upstream than at small friction coefficients. As a result the peaks in water level downstream of the contraction are broader for large n and show more reflections than for small n.

The behaviour of the water surface in this supercritical flow scenario is quite sensitive to bed slope. Figures 2.4.7 and 2.4.8 show the water surface level using several values of the bed slope ($n = 0.011$, 0.013 and 0.015) at constant Manning friction coefficient $n = 0.011$. An increase in the friction coefficient leads to an decrease of the initial wave angle ($\beta \approx 22\,\mathrm{deg}$ for $S_0 = 0.01$, $\beta \approx 20.3\,\mathrm{deg}$ for $S_0 = 0.05664$ and $\beta \approx 19.1\,\mathrm{deg}$ for $S_0 = 0.09$). As a consequence the frequency of the peaks along the centerline and along the wall is higher at small bed slopes than at big bed slopes. At $S_0 = 0.09$ the peaks in water height are rapidly damped and the second reflection on the centerline is of reduced amplitude. This is because the first reflection on the wall is located near the throat of the contraction and is thus strongly damped by the negative wave front. At $S_0 = 0.01$ the Froude number tends to stabilize around 1.7 whereas at $S_0 = 0.09$ the supercritical nature of the flow is more evident.

2.4.3 Irregular shock reflection

The previous two configurations showed regular shock reflections (RR) at the wall and on the channel axis. This corresponds to configurations ⓐ and ⓑ on Fig. 2.4.9 and appears at high Froude numbers and low deflection angles θ.
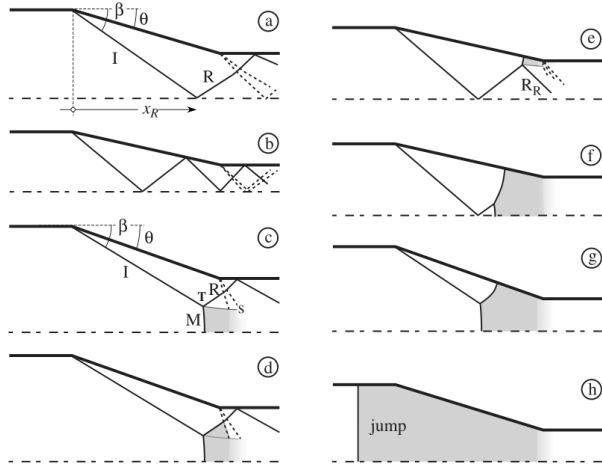
Figure 2.4.9: Irregular shock reflection - Different shock wave patterns in a linear channel contraction. Solid lines denote shock wave fronts, dashed lines denote the fan originating at the downstream edge of the contraction; shaded area denotes subcritical flow. I and R are the incident and reflected shock, M is the Mach stem. Figure from Defina [18].

A second category of shock reflection is the irregular one (IR). This corresponds to configurations ⓒ and ⓓ on Fig. 2.4.9 in the case of an IR off the channel axis and to configuration e for an IR off the converging wall. The IR can be either weak or strong and shows three shock waves (incident I, reflected R and Mach stem M) meeting at the triple point T. A contact discontinuity, the slip stream s, also originates at the triple point, and separates the flow behind the reflected shock from the flow behind the Mach stem. Across the slip stream water depth is continuous while flow velocity (hence, the Froude number) is discontinuous.

Because of the obvious symmetry of the flow, only one half of the channel is meshed and computed. Let's take the same geometry as Defina [18] with the ratio of channel widths $b_3/b_1 = 0.3$ and the deflection angle $\theta = 15\,\mathrm{deg}$. The channel has a flat bottom (bed slope $S_0 = 0$) and the flow is inviscid (no friction). On Fig. 2.4.10, the Froude number at the inlet is decreased from $Fr = 4.20$ to $Fr = 4.10$. In this configuration, one gets the configuration e on Fig. 2.4.9. Until $Fr = 4.15$, one has two strong IRs off the converging wall and the channel axis and two facing pockets of subcritical flow across the throat. At $Fr = 4.10$ the subcritical regions increase in size and

finally merge forming one single stable band of subcritical flow all across the throat. Only one IR is present near the converging wall, the shock pattern near the channel axis does not have a reflected shock. Lowering further the Froude number triggers an unstable transition to flow configuration with a 2D jump in the contraction or a normal jump upstream of the contraction (case (h)). The shapes of the results is very similar to those in Defina [18].
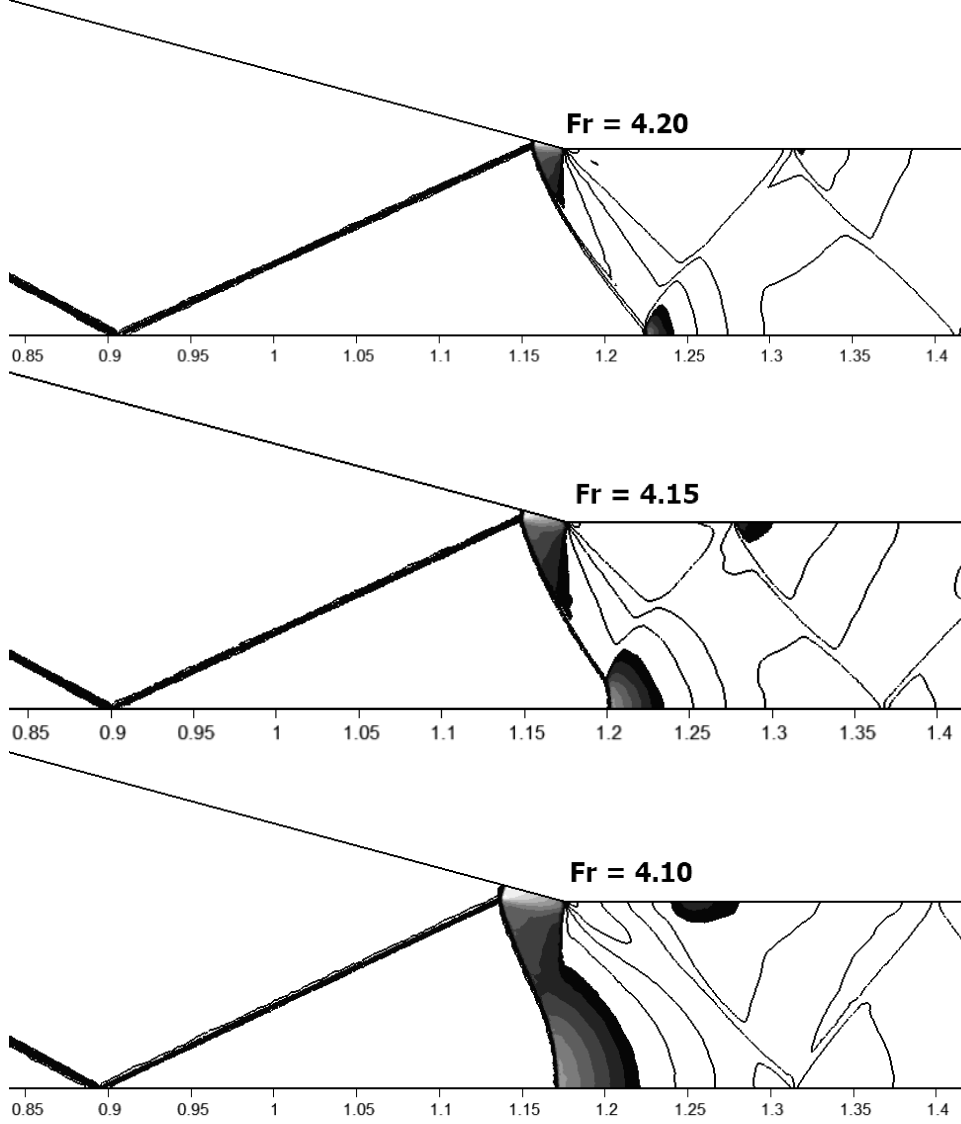
Figure 2.4.10: Steady configuration with an IR off the converging wall ($\theta = 15\,\mathrm{deg}$ and $b/B = 0.3$): from top to bottom $Fr = 4.20$, $Fr = 4.15$ and $Fr = 4.10$. $Fr = 4.15$ has two strong IRs off the converging wall and the channel axis and two facing pockets of subcritical flow across the throat. $Fr = 4.10$ has one stable band of subcritical flow all across the throat. Isolines of Froude number and highlight of the subcritical areas.

2.5 Transcritical flow in long channels

Let us consider a transcritical flow past a mild contraction in a long channel. The channel geometry is depicted in Fig. 2.5.1: a long channel with a width b_1 shows a symmetric contraction characterized by the length and width of the narrowest section b_2 and L_b respectively and by the
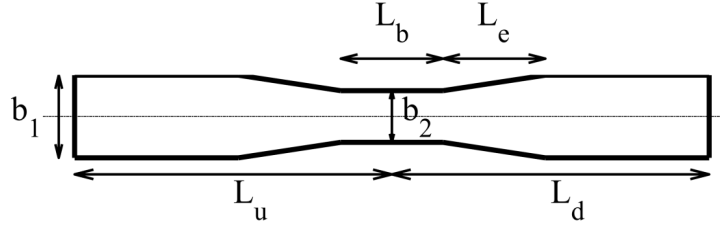
Figure 2.5.1: Transcritical flow in long channels - Geometry of the flow.

length of the symmetric contracting/expanding sections L_e. The distance between the upstream inlet boundary to the contraction is L_u, the steady flow discharge is Q and the channel bed slope is S_0.

2.5.1 Theoretical 1D model

Assuming uniform velocity across the channel width, hydrostatic pressure and steady-state flow conditions, we model gradually varied flow in channels of constant slope and discharge Q, using Bresse's extension of Eq. (2.3) to nonprismatic geometries of the 1D momentum equation

$$\frac{dh}{dx} = \frac{S_0 - S_f + \frac{Q^2}{gA^3}\frac{\partial A}{\partial x}}{1 - \frac{Q^2 b}{gA^3}} \tag{2.17}$$

$$S_f = \left(\frac{nV}{R^{2/3}}\right)^2 = \left(\frac{nQ(b+2h)^{2/3}}{(bh)^{5/3}}\right)^2$$

Herein x is the distance along the bottom of the channel and b is the local top channel width. Rectangular cross-sections are used in the present case so that $A = bh$ and the partial derivative $\partial A/\partial x = h\partial b/\partial x$.

The channel operates under mild slope conditions: the overall hydraulic control is exerted from downstream to upstream sections and undisturbed flow is subcritical. Geometrically, we consider long channels where the total discharge is known, and with free overfall conditions at the outlet. For hydraulically long channels, where the contraction is sufficiently far form the outlet, the water surface reaches the contraction with uniform depth, y_n. For finite, hydraulically short channels, the specific energy and depth at the downstream end of the contraction (point A in Fig. 2.5.2) are determined by upstream integration of Eq. (2.17), with initial condition $h = y_c$ at the outlet of the channel. The resulting backwater curve approaches y_n asymptotically from the critical depth — it is a M2 profile.

To reconstruct the water profile in transcritical scenarios, we begin by identifying the control section inside the channel contraction; that is, the upstream-most section where critical depth is observed. In the present case, the control section corresponds to the downstream edge of the narrowest segment of the contraction (point A in Fig. 2.5.2). Hydraulic control dictates that we must integrate Eq. (2.17) forward, with initial condition $h = y_c$, ending at a hydraulic jump to the approaching M2 profile. We distinguish between the case in which the jump remains in the expansion zone (top of Fig. 2.5.2), and the lower-energy case in which the jump is expelled out of the channel constriction (bottom of Fig. 2.5.2). In either case the location of the hydraulic jump is identified as the intersection between the specific momentum functions of the M3 and M2 curves. The physical length and complex internal structure of the jump are neglected, so for a rectangular channel the location is at the unique point where the depth of the approaching M2 profile equals the conjugate of the upstream depth, $h_{u,conj}$. We use the hydraulic jump formula

25
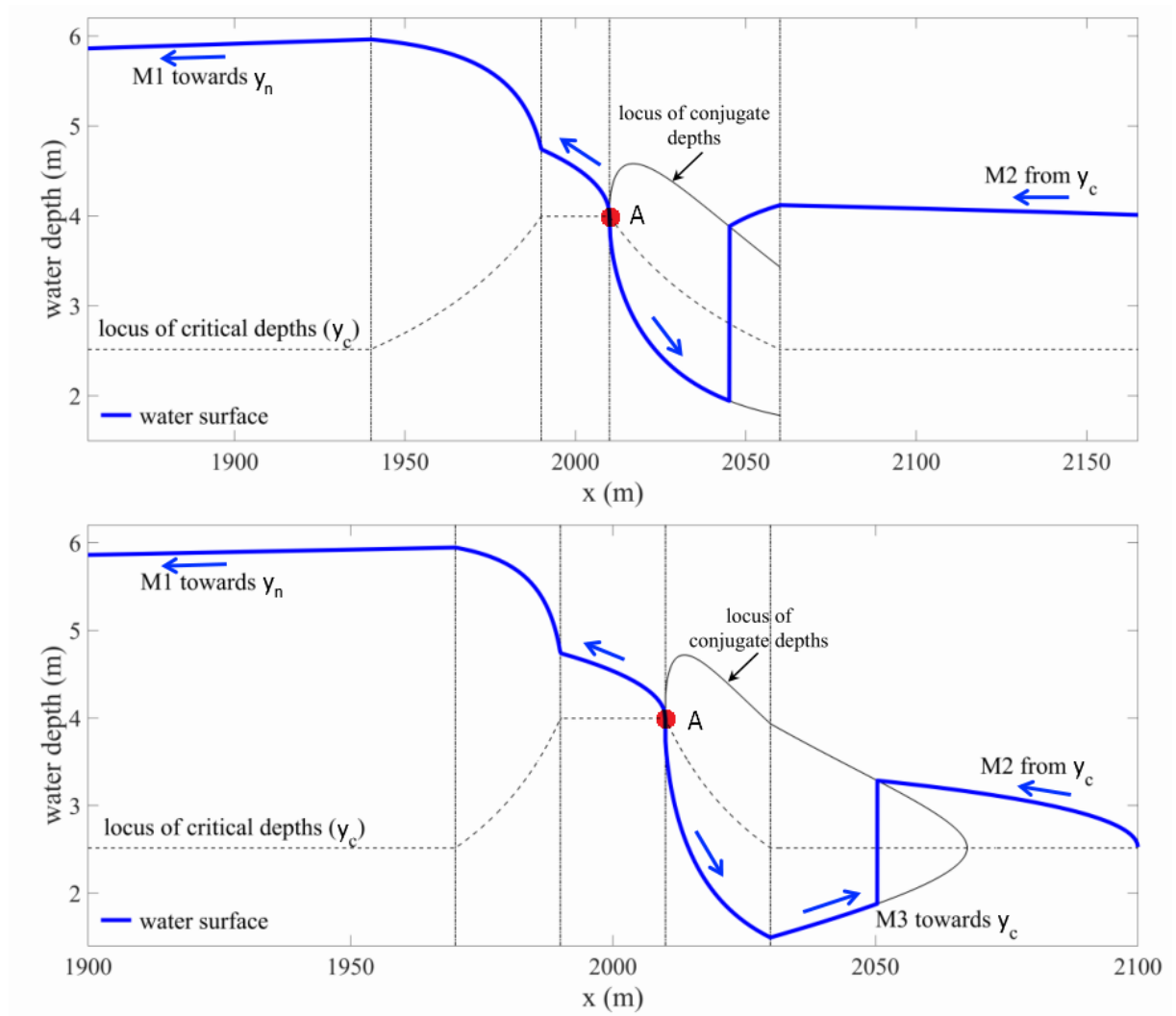
Figure 2.5.2: Transcritical flow in long channels - Construction of water surface profiles through the direction of integration of Eqs. (2.17). Figure from Cueto-Felgueroso [9]. (Top) Sample case where the hydraulic jump is contained within the expansion zone and (bottom) a sample case where the hydraulic jump is expelled outside of the expansion zone.
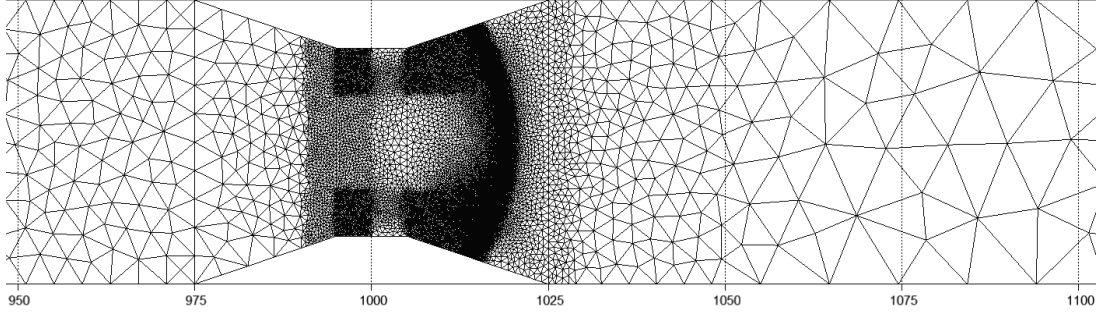
Figure 2.5.3: Transcritical flow in long channels - Mesh created after a first computation that located the hydraulic jump for $L_d = 250m$.

for rectangular channels:

$$h_{u,conj} = \frac{h_u}{2} \left(\sqrt{1 + 8Fr_u^2} - 1 \right) \tag{2.18}$$

where Fr_u is the Froude number computed with the upstream depth h_u. Upstream from the critical section the hydraulic control reverts to being exercised from downstream sections. Hence, the water profile is constructed through backwards integration of Eq. (2.17), with initial condition $h = y_c$ at point A. Upstream from the initial edge of the constriction we may observe either M1 or M2 profiles, depending on whether the normal depth is asymptotically approached from above or from below.

2.5.2 Results

To test a realistic outlet boundary condition, we compare the 1D and 2D model predictions for a mild contraction, $b_1 = 40m$, $b_2 = 26.5m$, same length of the converging/expanding sections, $L_e = 20m$, discharge $Q = 500m^3/s$, the channel bed slope is $S_0 = 0.002$. The Manning friction coefficient is $n = 0.04$ for the 2D computations and is $n = 0.0389$ for the 1D computations. Subcritical boundary conditions are imposed at the inlet ($h_{inlet} = y_n = 4.543m$, $u_{inlet} = Q/b_1 h_{inlet} = 2,751m/s$) and critical boundary conditions at the outlet ($h_{outlet} = y_c = 2.516m$). Several values of the distance to the outlet, L_d, where we imposed free overfall conditions. For this long channel, friction losses are large enough so that the available specific energy at the contraction is controlled by a backwater curve starting from the critical depth at the outlet. We induce the onset of transcritical flow at the throat section by reducing the distance to the outlet, L_d, from $4000m$ to $75m$ (see Figs. 2.5.4 and 2.5.5).

Extra care was taken during the generation of the 2D mesh. Indeed, as shown in Fig. 2.4.2, the capture of the hydraulic jump is crucial in the precision of the downstream section. Thus an initial computation allowed to detect the location of the hydraulic jump. A second mesh has then been built for each L_d with a refinement around the hydraulic jump (see Fig. 2.5.3 for the mesh for $L_d = 250m$). Both triangular and rectangular meshes were built for each value of L_d and their respective results were compared.

The 1D model predicts transcritical flow conditions for all the values of L_d. The 2D model predicts transcritical flow conditions for the smallest values of L_d whereas $L_d = 500m$ and $L_d = 4000m$ are near-critical (see Figs. 2.5.4 and 2.5.5). The hydraulically short channels ($L_d \leq 250m$) exhibit repelled hydraulic jumps that join at the middle of the section. The 1D computation for $L_d = 500m$ predicts a jump. On the opposite the 2D computation shows that the repelled hydraulic jumps do not meet at the middle of the section but remain near the side walls. This behaviour is similar to the theoretical curve for $L_d = 4000m$ where the height reaches the critical depth y_c at point A and then follows the M1 towards the uniform depth
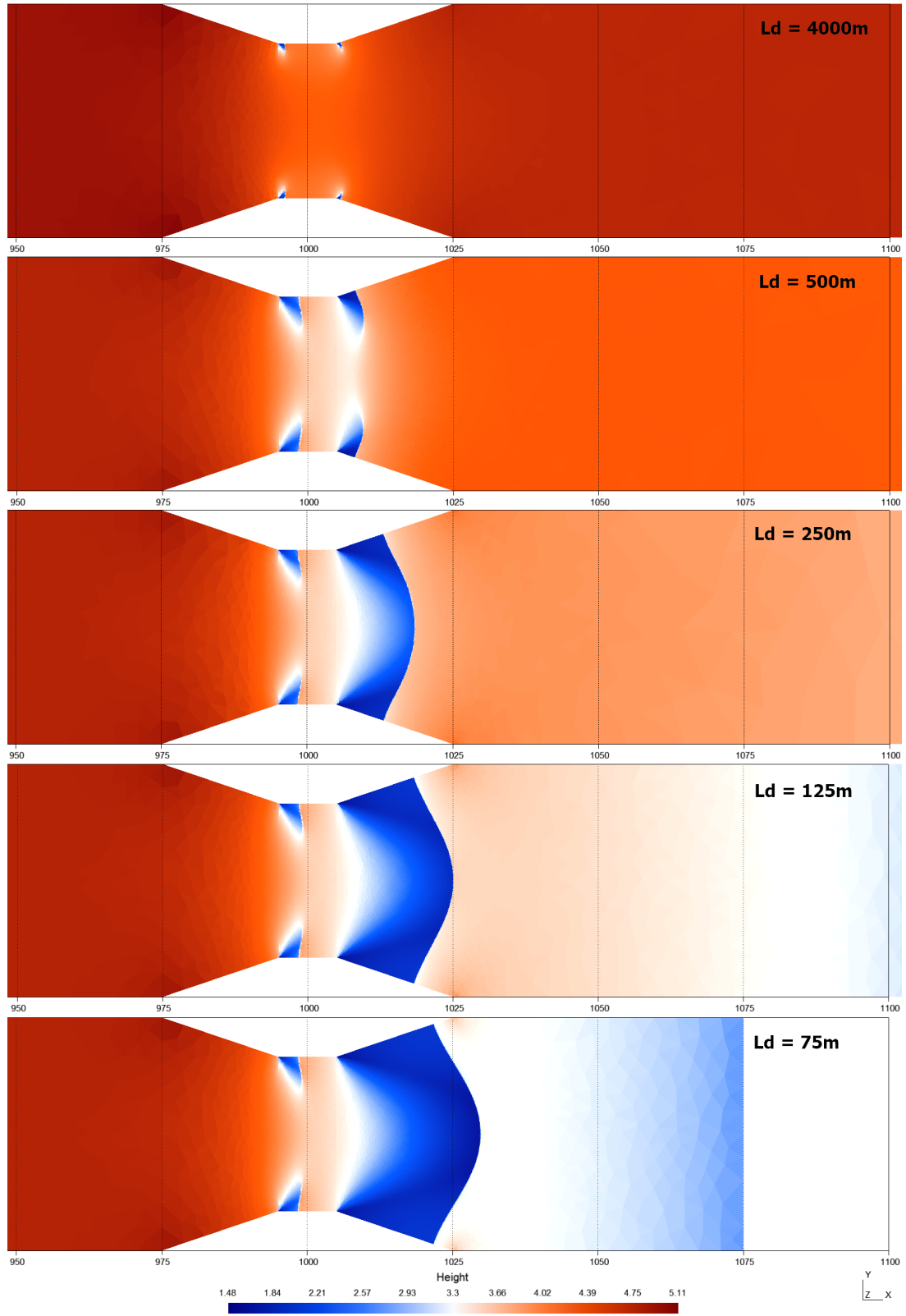
Figure 2.5.4: Transcritical flow in long channels - Onset of transcritical flow in the 2D model by reducing the distance to the outlet L_d from (top) $4000m$ to (bottom) $75m$.
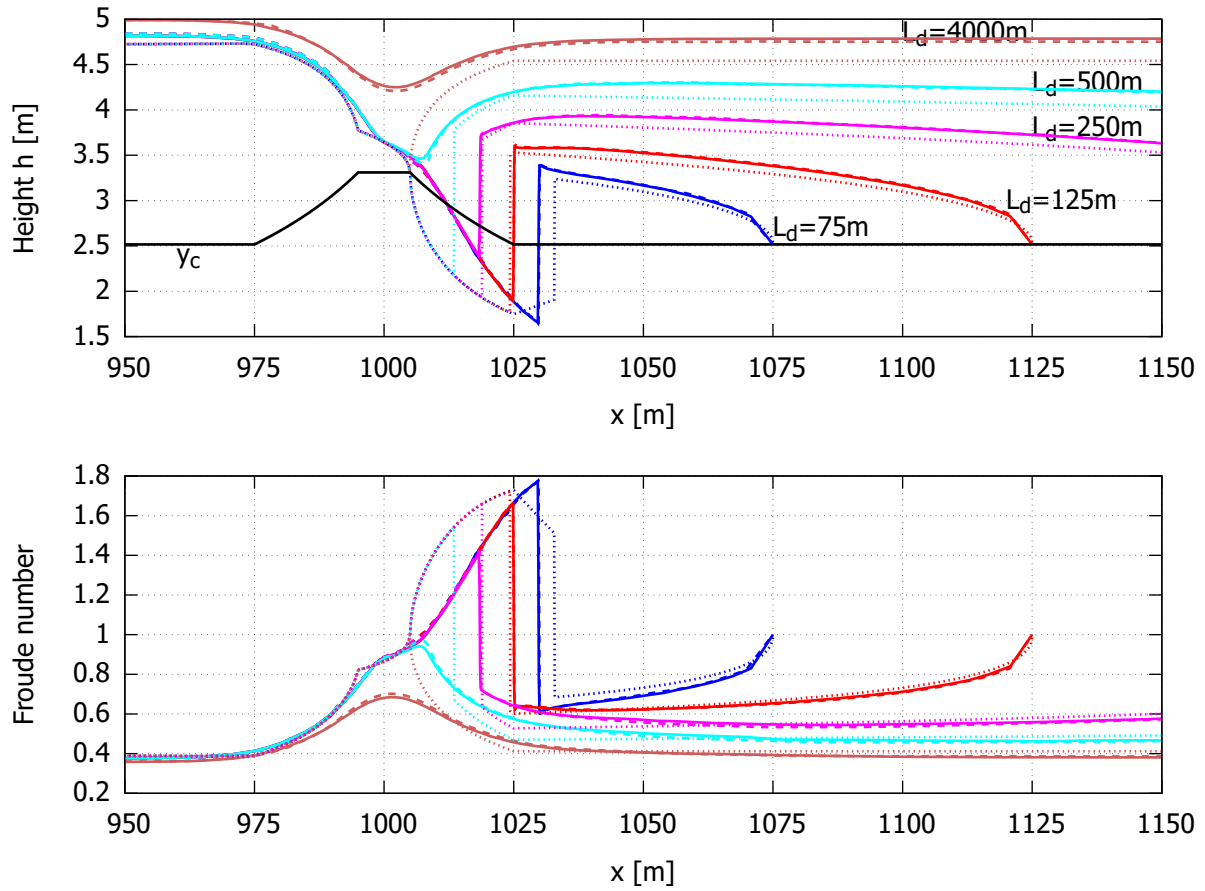
Figure 2.5.5: Transcritical flow in long channels - Onset of transcritical flow in the 1D (dotted lines) and 2D models based on a triangular mesh (full lines) or on a rectangular mesh (dashed lines) by reducing the distance to the outlet L_d. (top) Height and (bottom) Froude number.

y_n. The location of the hydraulic jump and the M1-M2 curves are very similar between the 1D and 2D models. However a discrepancy exists between these models inside the contraction for the gradually varied water surface profile leading to the toe of the jump. Indeed large Froude number conditions lead to flow patterns dominated by oblique shocks that render the 1D analysis invalid in the expansion zone. The discrepancy is the highest for $L_d = 75m$ where the hydraulic jump has been expelled outside of the expansion zone. The 1D model predicts a M3 that goes up towards $h = y_c$ but the 2D model predicts a toe of the jump that continues its descent. The 2D models based on the triangular and rectangular meshes show very similar results. The most visible difference is for $L_d = 500m$ near $Fr = 1$.

2.6 Partial breach of a dam

This test case analyses an unsteady flow resulting from a partial dam break or the instantaneous opening of sluice gates. The breach is nonsymmetrical ato demonstrate analysis of a general case. The bathymetric term is not considered in this case (constant elevation of the ground). This unsteady flow does not have any analytical solution but it has been reported by Fennema and Chaudhry [19], Bermúdez *et al.* [5], Valiani *et al.* [11], Chaudhry [8] and Biscarini *et al.* [20].

The computational domain is depicted in Fig. 2.6.1. It contains a $200m \times 200m$ closed domain (only non-slip walls are present), the breach is $75m$ wide and the structure of the dam is $10m$
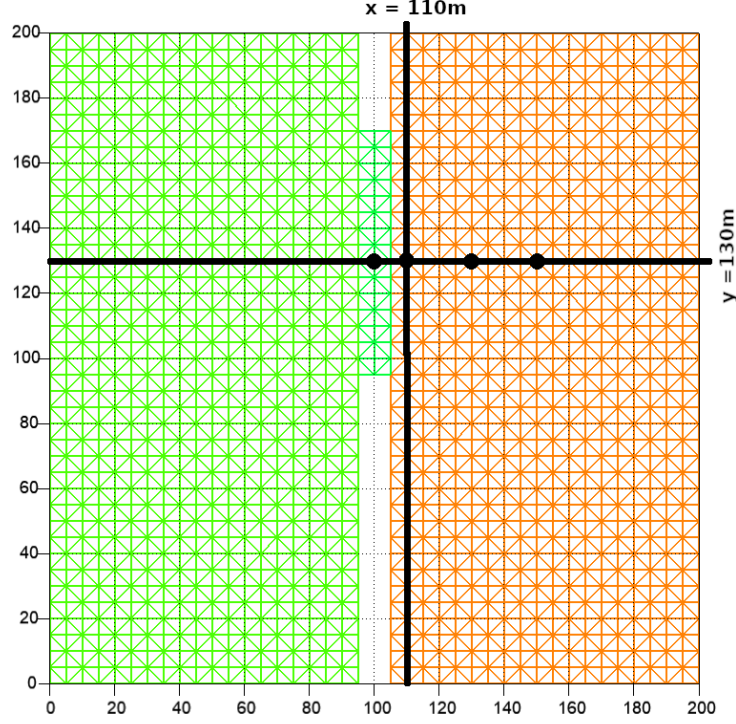
Figure 2.6.1: Partial dam breach - Geometry and mesh.

thick in the direction of the flow. The mesh is built from $5m \times 5m$ isosceles right triangles. The initial conditions are still water with a height of $10m$ in the left half and $5m$ in the right half (including the portion that models the dam/sluice gate).

The duration of the computation is $t = 7.2s$. At this time, the bore is well developed in the central portion and the wavefront has reached one bank of the channel. Figure 2.6.3 shows the three-dimensional water surface at the final time and Figure 2.6.2 shows iso-value lines of the water height and velocity arrays.

Figure 2.6.4 shows the computed water surface along cuts at $x = 110m$ and $y = 130m$. The numerical results from Fennema and Chaudhry [19] and from Biscarini *et al.* [20] and are also depicted for comparison. Fennema used a shallow water model solved with an implicit finite difference method. Biscarini used the 2D shallow water open-source code CCHE2-D and the full 3D Navier-Stokes multiphase equations implemented in OpenFOAM. The global shape of the height is in good agreement with the reference results. The 3D results from Biscarini show a water surface immediately upstream of the gate lower than those predicted by the shallow water codes because of the gravity force implemented in the full Navier-Stokes equations.

Figure 2.6.5 shows hydrographs at four different monitor points (these points are represented on Fig. 2.6.1). As underlined by Biscarini, the shallow water models tend to underestimate the water level and the frontwave celerity.
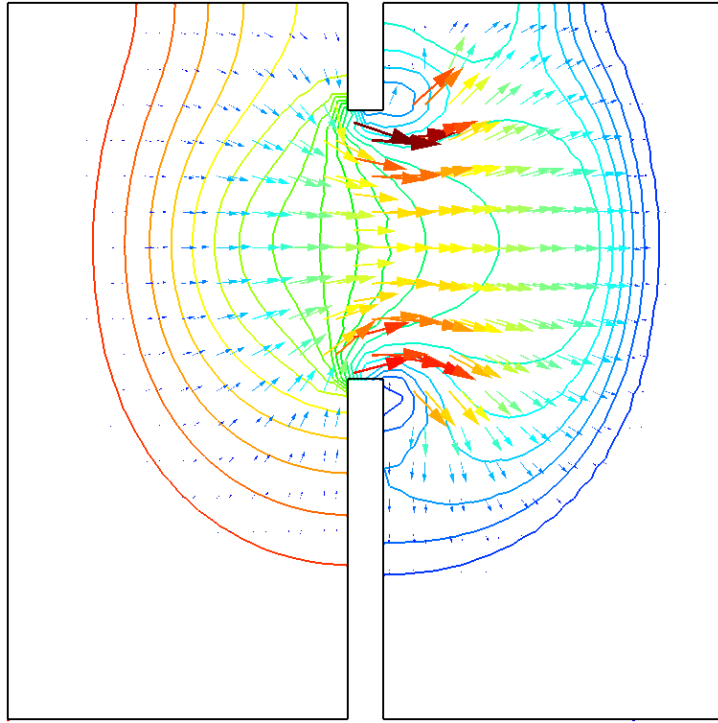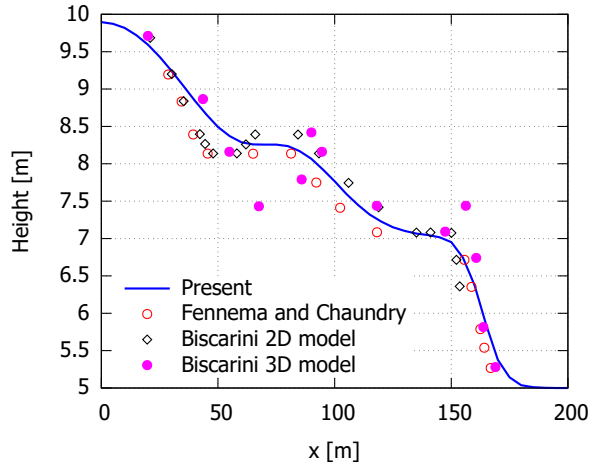
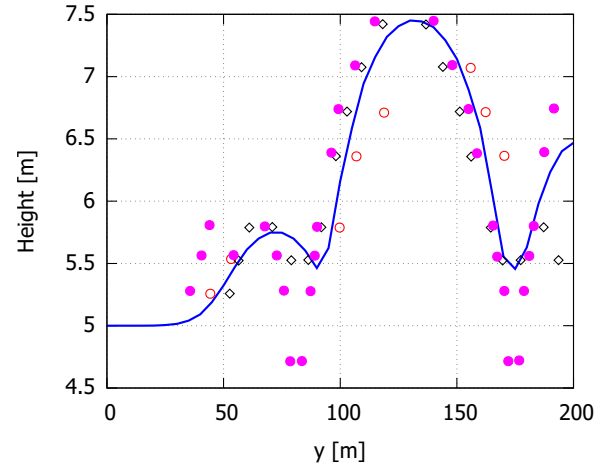**Figure 2.6.2:** Partial dam breach - Iso-value lines of the water height and velocity arrays at $t = 7.2s$.
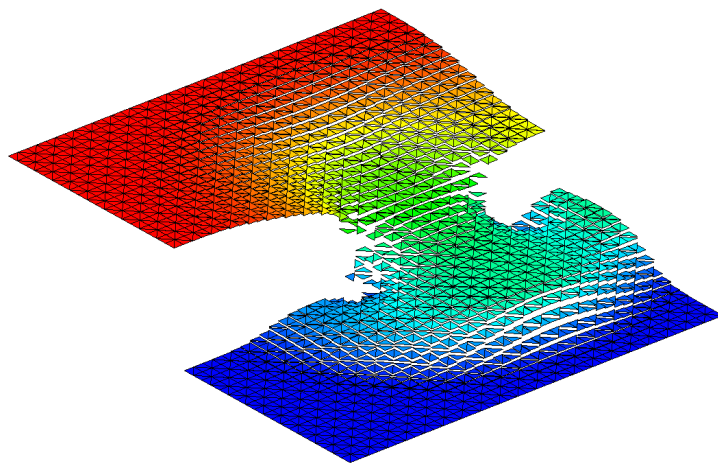
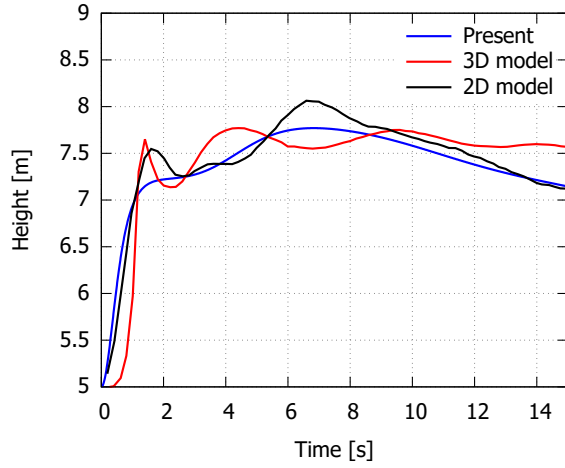**Figure 2.6.3:** Partial dam breach - Water surface at $t = 7.2s$.
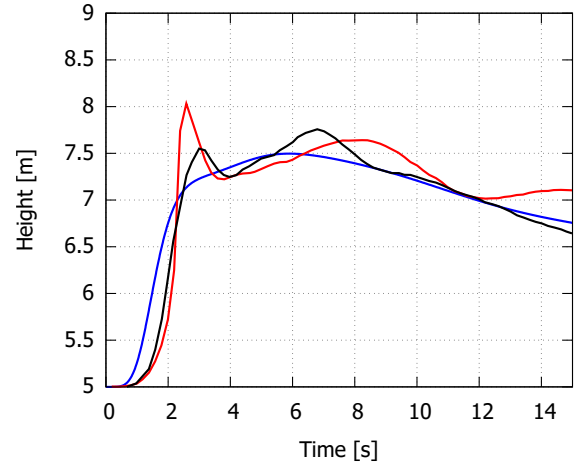
(a) Horizontal cut at $y = 130m$
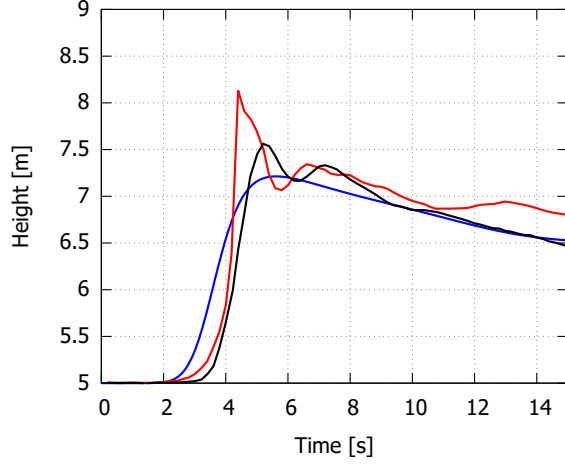
(b) Vertical cut at $x = 110m$

Figure 2.6.4: Partial dam breach - Water elevation 7.2s after the dam break. Comparison with the numerical results from Fennema and Chaundry [19] and from Biscarini *et al.* [20]
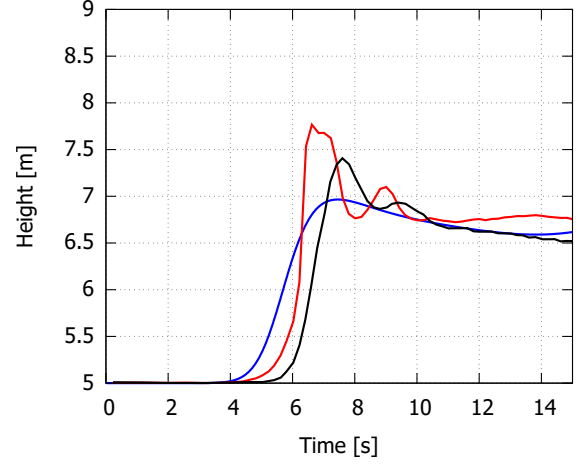
(a) Point at $(x = 100m, y = 130m)$

(b) Point at $(x = 110m, y = 130m)$

(c) Point at $(x = 130m, y = 130m)$

(d) Point at $(x = 150m, y = 130m)$

Figure 2.6.5: Partial dam breach - Water elevation as a function of time at four monitor points. Comparison with the numerical results from Biscarini *et al.* [20]

Bibliography

[1] de Saint Venant. Théorie du mouvement non permanent des eaux avec applications aux crues des rivières et à l'introduction des marées dans leur lit. *Comptes Rendus de l'Académie des Sciences de Paris*, 73:148–154, 237–240, 1871.

[2] V.T. Chow. *Open-Channel Hydraulics*. McGraw-Hill, Inc., New York, N.Y., 1959.

[3] P. Brufau and P. Garcia-Navarro. Two-dimensional dam break flow simulation. *International Journal for Numerical Methods in Fluids*, 33(1):35–57, 2000.

[4] B. van Leer. Towards the ultimate conservative difference scheme III. Upstream-centered finite-difference schemes for ideal compressible flow. *Journal of Computational Physics*, 23:263–275, 1977.

[5] A. Bermúdez, Dervieux A., J.-A. Désidéri, and Vázquez M.E. Upwind schemes for the two-dimensional shallow water equations with variable depth using unstructured meshes. Technical Report 2738, 1995.

[6] M.J. Castro, J.A. García-Rodríguez, J.M. González-Vida, and C. Parés. A parallel 2d finite volume scheme for solving systems of balance laws with nonconservative products. Application to shallow flows. *Computer Methods in Applied Mechanics and Engineering*, 195:2788–2815, 2006.

[7] C.-W. Shu and S. Osher. Efficient implementation of essentially non-oscillatory shock capturing schemes. Technical Report ICASE Report No 87-33, NASA, 1987.

[8] M.H. Chaudhry. *Open-Channel Flow, Second Edition*. Springer Science+Business Media, LLC, New York, NY, USA, 2008.

[9] L. Cueto-Felgueroso, D. Santillán, J.H. García-Palacios, and L. Garrote. Comparison between 2D shallow-water simulations and energy-momentum computations for transcritical flow past channel contractions. *Water*, 11(7):1476, 2019.

[10] T.H.Y. Yoon and S.-K. Kang. Finite volume model for two-dimensional shallow water flows on unstructured grids. *Journal of Hydraulic Engineering*, 130(7), 2004.

[11] A. Valiani, V. Caleffi, and A. Zanni. Finite volume scheme for 2D shallow-water equations. Application to the Malpasset dam-break. In *Proceedings of the 4th CADAM Meeting*. 18-19 November 1999, Saragozza, Spain, 1999.

[12] U.S. Army Corps of Engineers. Hydraulic design of flood control channels. Technical Report 1110-2-1601, Department of the Army, Washington D.C. 20314-1000, 1994.

[13] W. Lai and A.A. Khan. A discontinuous Galerkin method for two-dimensional shock wave modeling. *Modelling and Simulation in Engineering*, Article ID 782832, 2011.

[14] R.C. Berger and R.L. Stockstill. Finite-element model for high-velocity channels. *Journal of Hydraulic Engineering*, 121(10):710–716, 1995.

[15] H. Lee. Application of Runge-Kutta discontinuous Galerkin finite element method to shallow water flow. *KSCE Journal of Civil Engineering*, 18(5):1554–1562, 2014.

[16] A. Ippen and J.H. Dawson. Design of channel contractions. In *High-velocity flow in open channels: a symposium*, volume 116. Transactions of the American Society of Civil Engineers, 1951.

[17] C. Geuzaine and J.-F. Remacle. Gmsh: a three-dimensional finite element mesh generator with built-in pre- and post-processing facilities. *International Journal for Numerical Methods in Engineering*, 79(11):1309–1331, 2009.

[18] A. Defina and D.P. Viero. Open channel flow through a linear contraction. *Physics of Fluids*, 22:036602, 2010.

[19] R.J. Fennema and M.H. Chaudhry. Explicit methods for two-dimensional transient free-surface flows. *Journal of Hydraulic Engineering*, 116(8):1013–1034, 1990.

[20] C. Biscarini, S. di Francesco, and P. Manciola. CFD modelling approach for dam break flow studies. *Hydrology and Earth System Sciences*, 14:705–718, 2010.